OPTICAL AND MAGNETIC RESONANCE

CHARACTERIZATION OF POINT DEFECTS IN

LITHIUM NIOBATE AND LITHIUM TANTALATE

By

KEVIN LEE SWEENEY

Bachelor of Science

Oklahoma State University

Stillwater, Oklahoma

1980

Submitted to the Faculty of the
Graduate College of the
Oklahoma State University
in partial fulfillment of
the requirements for
the Degree of
DOCTOR OF PHILOSOPHY
December, 1984

OPTICAL AND MAGNETIC RESONANCE

CHARACTERIZATION OF POINT DEFECTS IN

LITHIUM NIOBATE AND LITHIUM TANTALATE

Thesis Approved:

Larry E. Halliburton
Thesis Adviser

Joel J Martin

J Paul Devlin

Norman N. Durham
Dean of the Graduate College

ii

1218546

ACKNOWLEDGEMENTS

TABLE OF CONTENTS

LIST OF TABLES

LIST OF FIGURES

CHAPTER I

INTRODUCTION

Lithium niobate and lithium tantalate are electro-optic materials that are useful in a variety of optical applications. These applications include nonlinear devices, linear electro-optic devices, and holographic devices. The property of these materials that is useful for the devices is an electric-field-induced change in the index of refraction. This change in the linear index of refraction is given by $\Delta n_3 = -(1/2) \cdot n_3^3 \cdot r_{33} \cdot E_3$ and allows for an optical-to-electrical coupling of systems. That is, an optical property of the material can be controlled electrically.

Lithium niobate has not been found in nature and was described for the first time by Zachariasen[1] in 1928. Widespread use of the material did not begin until 1965 when Ballman[2] reported the successful growth of single crystals of $LiNbO_3$ by the Czochralski technique. The melting points of $LiNbO_3$ and $LiTaO_3$ are 1260°C and 1560°C and their Curie temperatures are 1197°C and 620°C, respectively. The point symmetry of both crystals is C_{3v} and Figure 1 shows the positions of the ions for a portion of the lattice above and below the Curie temperature, T_c.

LITHIUM NIOBATE CRYSTAL STRUCTURE
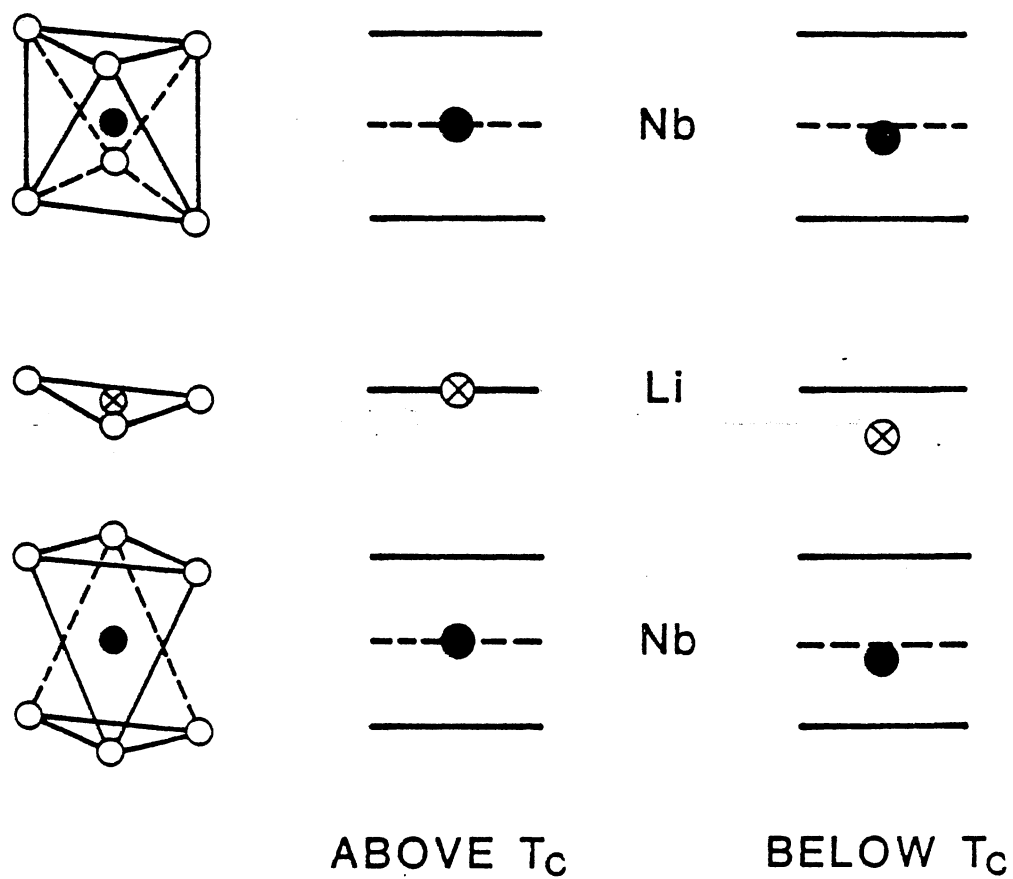
ABOVE T_C BELOW T_C

Figure 1. Crystal structure of $LiNbO_3$ above and below the
Curie temperature T_C

The crystal structure above T_c consists of a collection of oxygen octahedra with the centers of the octahedra being occupied by Nb ions. These oxygen octahedra are separated by a layer of oxygen and lithium ions. Below the Curie temperature the crystal structure becomes distorted as the ions are displaced along the c axis. This distortion leaves the centers of the oxygen octahedra being occupied by the repeating sequence of Li, Nb, and vacancy along the crystal's c axis.

Optical applications of these materials are plagued by light-induced inhomogeneities called "optical damage". This optical damage, usually referred to as the photo-refractive effect, is caused by successive excitation and retrapping of electrons. As a light beam propagates through the crystal, electrons are excited and eventually are trapped around the periphery of the beam, thus setting up a space charge. This space charge, which is determined by the concentration and location of trapping sites, changes the index of refraction by the linear electro-optic effect. These non-uniform index changes limit the usefulness of the materials.

Research efforts to identify the defects responsible for the damage have pointed to impurities. Iron is one such impurity present in the part- per-million range in these materials. The model

$$hv + Fe^{2+} = Fe^{3+} + e^-$$
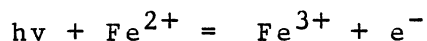
was proposed by Glass et al.[3] for the optical damage

mechanism. The electron released from the Fe^{2+} ion becomes trapped at an Fe^{3+} ion, thus iron acts as both the source and the trap.

An understanding of the point defects in $LiNbO_3$ and $LiTaO_3$ will be necessary for improvements in the performance of devices made from these materials. However, the knowledge of the defect structure of lithium niobate and lithium tantalate is in the early stages. Schirmer and von der Linde[4] identified two point defects in $LiNbO_3$, a radiation-induced hole center and a Nb^{4+} center. They suggested that the Nb^{4+} center was a self-trapped electron at a niobium ion occupying a normal site in the lattice. Other workers have identified impurities such as Fe^{3+}, Cr^{3+}, Mn^{2+}, and Gd^{3+} in $LiNbO_3$ by ESR.[5-11]

$LiNbO_3$ and $LiTaO_3$ can have large deviations from the stoichiometric composition. A parameter that is commonly used to characterize the non-stoichiometric crystal is the Li/Nb ratio. Little is known about the defect structures that allow for these large deviations in stoichiometry. Nassau and Lines[12] proposed a stacking disorder along the c axis, such as the replacement of a Li-Nb-Li sequence by a Nb-Li-Nb sequence.

Another type of defect is produced by reduction. Early investigators found that heating the crystals in an oxygen-deficient atmosphere will turn them "black", but little was known about the defects produced during such reductions. One phase of this dissertation will be to

expand on previous efforts to understand the defects produced by radiation and reduction in undoped $LiNbO_3$ and $LiTaO_3$.

Efforts to reduce or even eliminate the optical damage problem have focused both on purification of the starting material used in the crystal growth and in post-growth treatments such as oxidation[13] or electro-diffusion.[14] Recently, Bryan et al.[15] reported that resistance to optical damage in $LiNbO_3$ is improved if more than 4.5 % MgO is added to the melt. Their systematic investigation included crystals with a variety of Mg-doping levels and Li/Nb ratios, and they demonstrated the existence of a threshold effect with regard to Mg doping. Improved extinction ratios and operation at higher power densities were achieved in devices fabricated from the more heavily doped material. Bryan et al.[15] showed that the improved performance was due to a significant increase in the photoconductivity.

The second phase of this dissertation is to characterize the reduction and radiation properties of Mg-doped lithium niobate. Crystals with different Mg-doping levels and with different Li/Nb ratios are compared to undoped material.

CHAPTER II

EXPERIMENTAL PROCEDURES

The undoped single crystals of $LiNbO_3$ and $LiTaO_3$ used in this study were obtained from Crystal Technology, Palo Alto, CA and from Union Carbide, San Diego, CA. The $LiNbO_3$ crystals were divided into three groups depending on their quality. These classes were high purity, optical quality, and acoustic. Our $LiTaO_3$ crystals did not have a purity classification. The magnesium-doped $LiNbO_3$ samples used in this study were grown by Crystal Technology for McDonnell Douglas. These samples consisted of a series of magnesium doping levels and stoichiometries. The Mg-doping levels were 3%, 5%, 7%, and 9% MgO in the melt. At each doping level, crystals with different stoichiometries were grown, which included lithium-deficient samples with 46.5 % Li, congruent samples with 48.5 % Li, stoichiometric samples with 50 % Li, and lithium-rich samples with 51.5 % lithium in the melt.

Optical absorption data were taken using a Perkin-Elmer 330 or a Cary 14 spectrophotometer. A set of matched Glan-Thompson polarizers were used for some of the optical absorption measurements. For optical

6

measurements below room temperature, two types of Dewars were used. Data at 10 K were obtained using a Sulfrian Dewar and at 85 K using a liquid-nitrogen Dewar built by the Instrument Shop at Oklahoma State University. The samples were cut with a diamond saw to dimensions of 15 x 10 x 1.5 mm^3 and were manually polished to an optical surface quality using Buehler, Ltd. silicon carbide powder and 9, 7, 3, and 1 micron diamond paste.

Electron spin resonance (ESR) measurements were made using a Varian 4501A ESR spectrometer or a Bruker E200D spectrometer. Both ESR spectrometers operated at 9.30-GHz microwave frequency and 100-KHz magnetic field modulation frequency. ESR measurements at 77 K were made by using a finger Dewar which enabled the sample to be placed directly in liquid nitrogen. The finger Dewar consisted of a quartz tube which could be placed in the microwave cavity and was constructed by the Glass Shop at Oklahoma State University. An Air Products Heli-tran gas flow system or a Varian nitrogen gas flow system was used for low-temperature thermal anneals. Controlled temperatures between 8 K and 300 K were possible with the Air Products helium gas flow system and temperatures between 80 K and 300 K with the Varian nitrogen gas flow system. Sample size was typically 2 x 3 x 10 mm^3 for the ESR measurements.

Thermoluminescence and x-ray-induced luminescence data were obtained using an optical system that consisted

of an RCA C31034 photomultiplier tube, a Keithley 600B
electrometer, and a Spex 0.25-m monochromator with a
grating blazed at 500 nm. The x-rays were produced with
a Machlett OEG-60 x-ray tube (tungsten target) operating
at 35 kV and 30 mA. No instrumental spectral response
corrections have been made to the luminescence data. The
temperature in these luminescence experiments was
controlled by an Air Products closed-cycle helium
refrigerator.

A 2.0-MeV Van de Graaff accelerator operating in the
electron mode was used to produce defects for most of the
ESR and optical absorption measurements. Samples of
$LiNbO_3$ or $LiTaO_3$ cracked when placed directly in the
electron beam. Since the crystals are ferroelectric, the
cracking presumably was caused by the high internal
electric fields generated by the electron beam. To avoid
this cracking problem, x-rays obtained by scattering the
high-energy electrons from a copper block were used for
defect production. The total dose received by a sample
during irradiation was approximately 1 MRad (Si).

Another technique used for defect production was
reduction. One method of reducing was heating the sample
in a vacuum of approximately 10^{-5} Torr. A Hoskins tube
furnace capable of temperatures up to $1100^{\circ}C$ was used.
The vacuum system consisted of a diffusion pump connected
to a fused-silica tube. The fused-silica tube outgased
for an extended period of time when placed in the

furnace, thus limiting the effectiveness of this method for reduction. This system containing the fused-silica tube could reduce $LiNbO_3$ but proved inadequate to reduce $LiTaO_3$ to the desired optical absorption coefficients. A more efficient reduction system consisting of a stainless-steel tube extending into the furnace and either an argon or hydrogen atmosphere was necessary for the $LiTaO_3$ reductions.

An Oriel Universal Arc lamp, Model 8500 with a 150-W xenon bulb, was used for the optical bleachings in this study.

CHAPTER III

EXPERIMENTAL RESULTS

Irradiation of $LiNbO_3$ and $LiTaO_3$

Radiation-induced defects in $LiNbO_3$ and $LiTaO_3$ have
been studied by optical absorption and electron spin
resonance (ESR) techniques. Figure 2 shows the optical
absorption spectrum of $LiNbO_3$ at 85 K for π (E parallel
to the crystal's c axis) and σ (E perpendicular to the
crystal's c axis) polarizations after an 85 K x-
irradiation of approximately 1 Mrad (Si). As-grown
$LiNbO_3$ is transparent up to approximately 310 nm. After
the irradiation, the σ-polarized absorption peaks near
500 nm with a shoulder at approximately 800 nm. The
π polarization shows only the 500-nm peak.

The ESR spectra of $LiNbO_3$ taken at 77 K after an x-
irradiation at 77 K is shown in Fig. 3. Two spectra are
produced by the irradiation. One is a holelike resonance
at g_c = 2.0294 and the other is a broad electronlike 10-
line hyperfine pattern. The sharp ESR spectrum has been
assigned by Schirmer and von der Linde[4] to a hole trapped
on an oxygen ion, and they have assigned the 10-line
hyperfine pattern to an electron trapped on a Nb^{5+} ion.

10
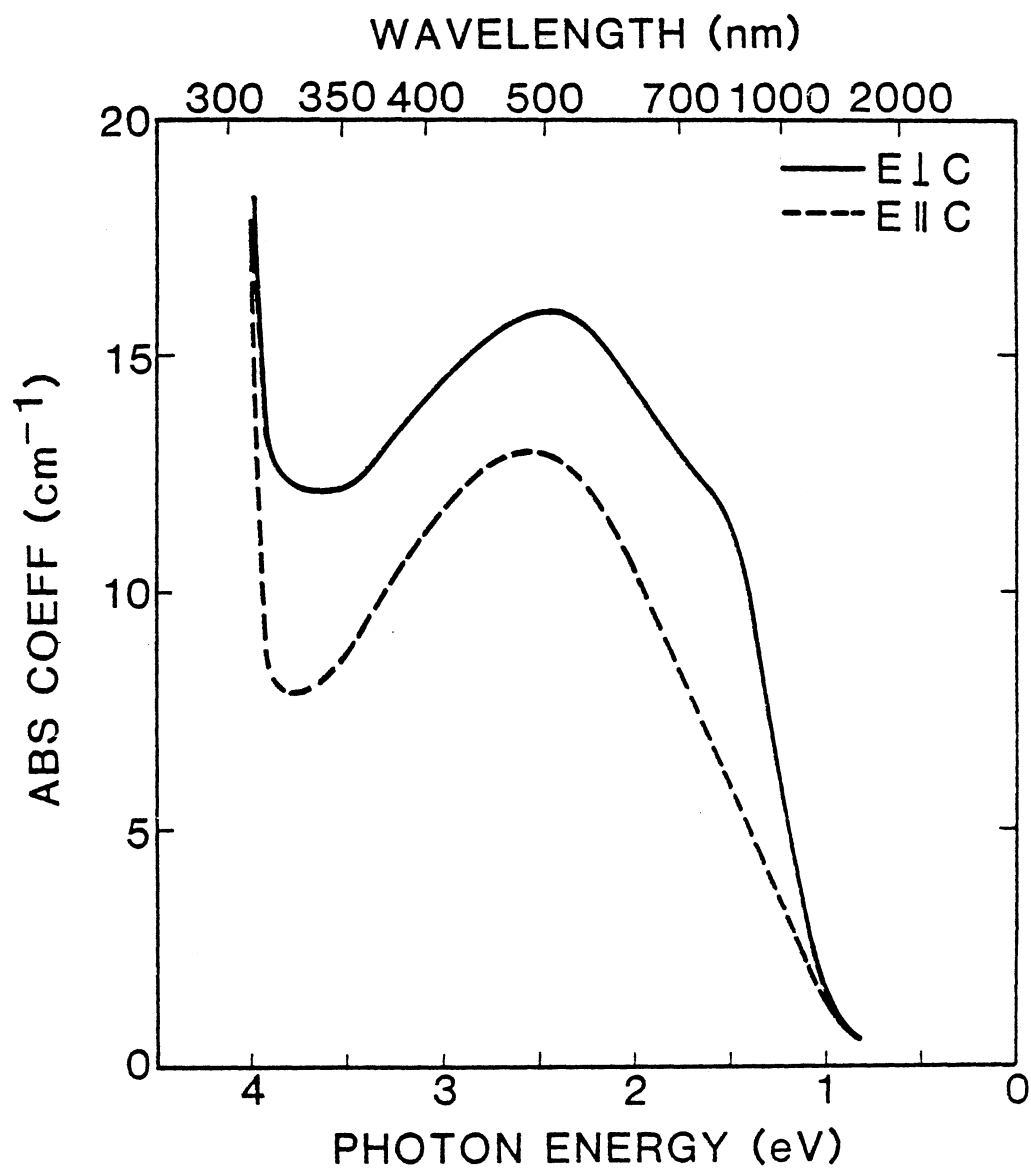
Figure 2.   Optical absorption of LiNbO$_3$ at 85 K after an x-irradiation at 85 K

1000   3000   5000   G

Figure 3.   ESR spectrum of LiNbO$_3$ taken at 77 K after an
            x-irradiation at 77 K

The ten lines are from an interaction with the $I = 9/2$, 100% abundant ^{93}Nb nucleus. An interesting feature of Fig. 3 is the apparent inequality in the concentrations of the hole center and the Nb^{4+} electron trap. Although no quanitative measurements were made, it is seen that a double integration of the hole center would be much larger than a similar integration of the Nb^{4+} spectrum. This difference in concentrations of paramagnetic centers is common in our $LiNbO_3$ crystals and indicates a significant number of unobserved electron traps must be present after irradiation.

To establish a correlation between the optical absorption shown in Fig. 2 and the ESR spectra of Fig. 3, the thermal decays of the defects were investigated. Shown in trace (b) of Fig. 4 is the intensity of the ESR holelike spectra during a pulse anneal. Each anneal step consisted of holding the sample for 5 minutes at the desired temperature and then returning to 85 K where the remaining intensity was measured. Trace (a) in Fig. 4 shows the corresponding intensity of the irradiation-induced optical absorption (σ polarization) band of Fig. 2 during a similar thermal anneal. The experimental conditions for the anneal of the optical peak were the same as in the thermal anneal of the ESR spectrum. Figure 4 indicates a correlation between the holelike ESR spectrum of Fig. 3 and the 500-nm optical absorption band in Fig. 2.
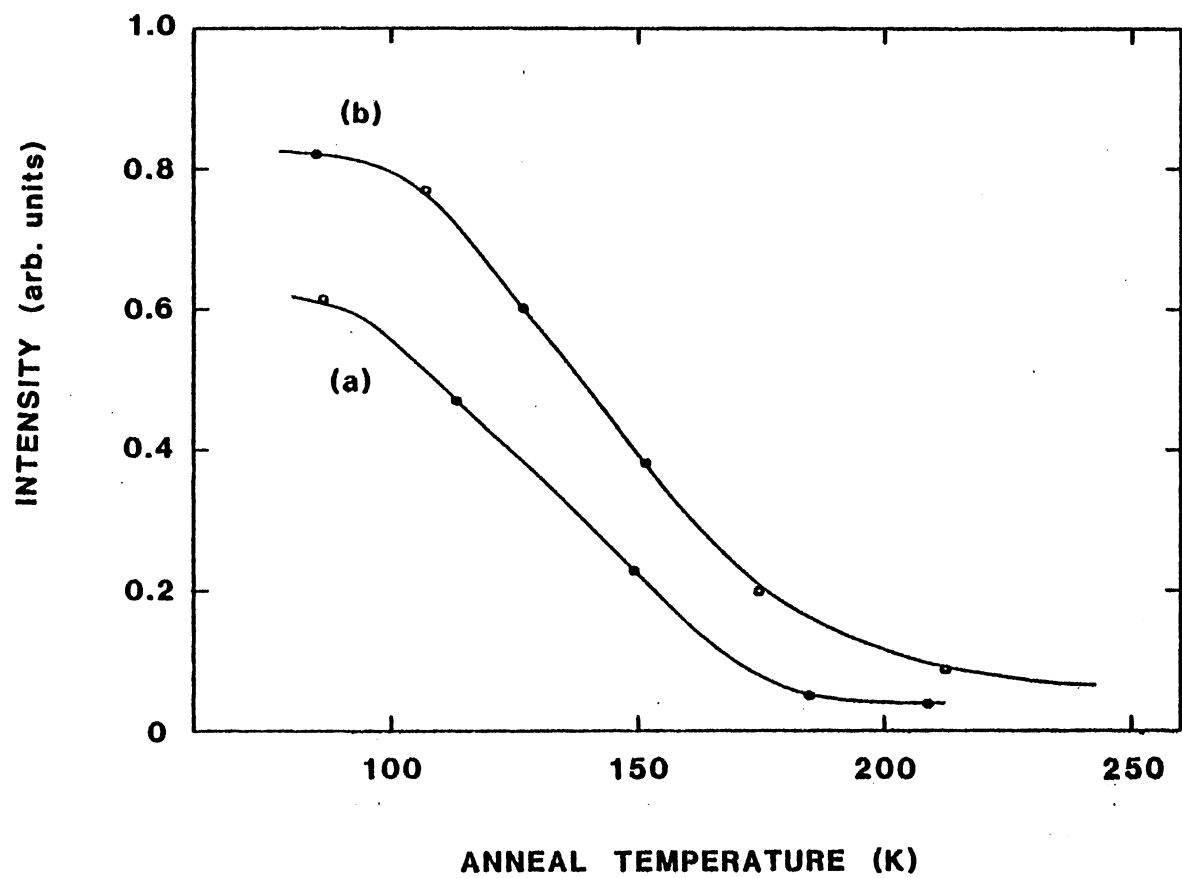
Figure 4. Thermal anneal behavior of the (a) hole center
optical band and (b) the ESR hole center in LiNbO$_3$
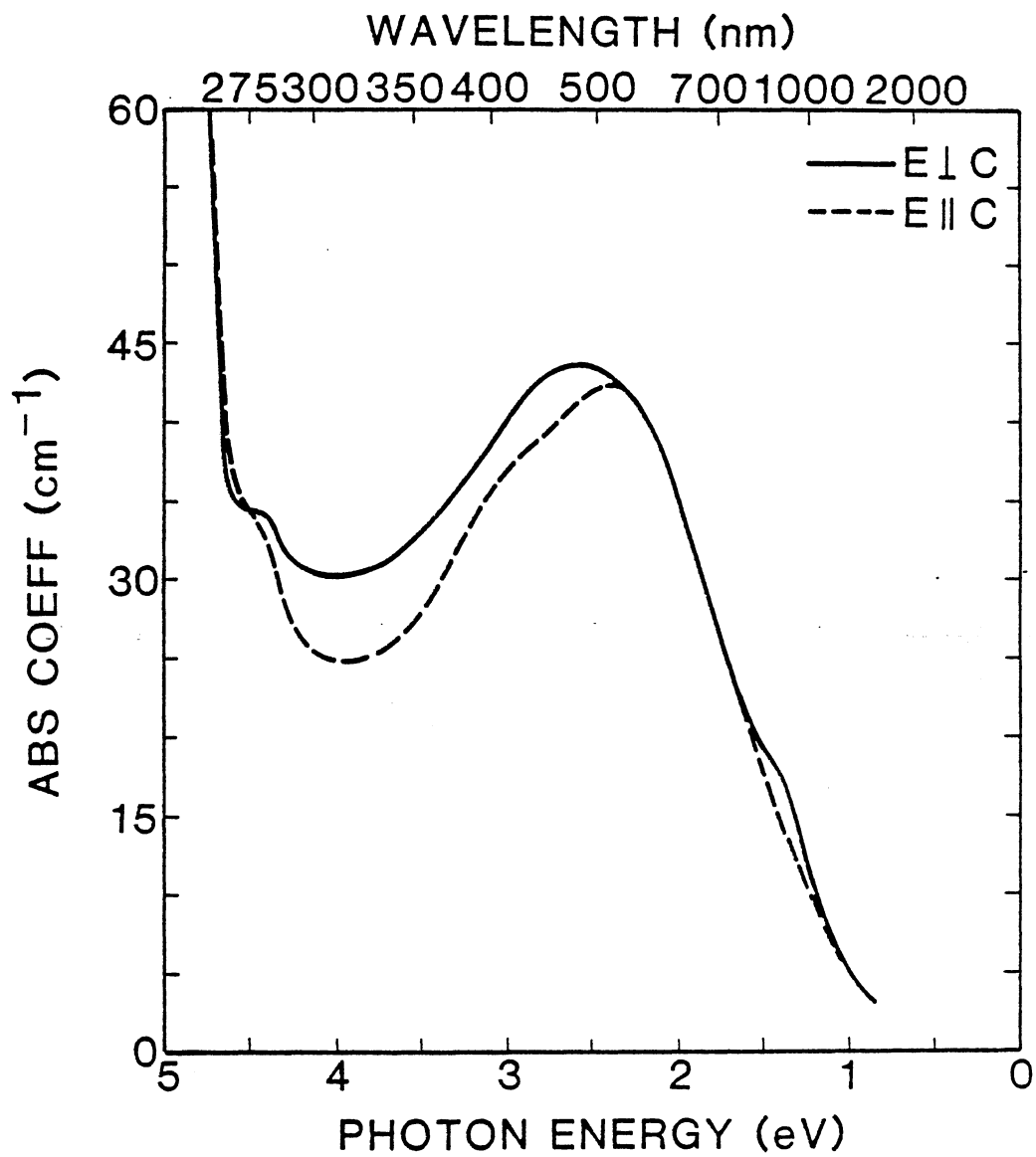
Figure 5. Optical absorption of LiTaO$_3$ at 85 K after
an x-irradiation at 85 K

A set of x-irradiation experiments identical to those presented above for $LiNbO_3$ were carried out for $LiTaO_3$.[16] Figure 5 shows the optical absorption data for both polarization directions taken at 85 K for $LiTaO_3$ after an 85 K x-irradiation. The radiation produces a band near 470 nm (2.64 eV). One interesting feature of the σ polarization is a shoulder at approximately 1.4 eV, since a similar band is also observed in $LiNbO_3$ at 1.6 ev after the x-irradiation. The appearance of these small bands after an irradiation and (as will be presented later) broad optical bands at these same wavelengths after reduction suggests assigning these two bands to electron traps Nb^{4+} and Ta^{4+}, respectively.

The ESR spectra for $LiTaO_3$ taken at 17 K after an x-irradiation of approximately 1 Mrad (Si) at 77 K is shown in Fig. 6. Both traces in Fig. 6 are broken near 3700 gauss. The high-field portion of the spectrum was taken with the spectrometer's gain ten times higher than the gain used for the low-field portion of the trace. Trace (a) was taken with the magnetic field parallel to the c axis and the holelike spectrum at 3300 gauss is resolved into a three-line pattern with g_c = 2.0224. The intensities of the three lines are approximately in the ratio 1:2:1. Also, the three lines are equally spaced in field with separation between adjacent lines being approximately 52.5 gauss. Together, these observations suggest that the three lines arise from a hyperfine
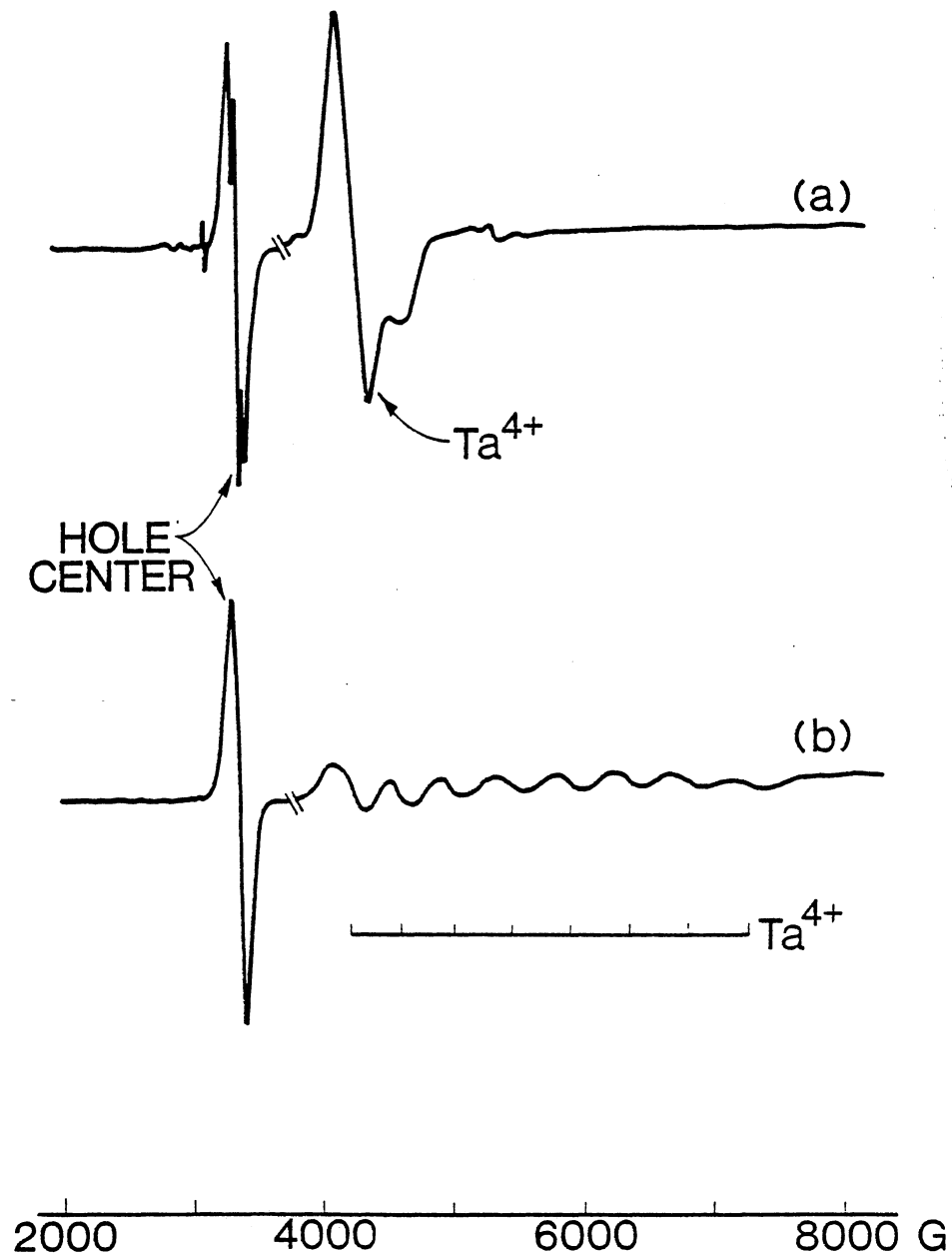
Figure 6. ESR spectra, taken at 17 K, from $LiTaO_3$ x-irradiated at 77 K, with the magnetic field (a) parallel and (b) perpendicular to the crystal's c axis

interaction with two equivalent 100% abundant I = 1/2 nuclei. A proton would be a resonable candidate for these nuclei.

The spectrum near 4000 gauss in trace (a) of Fig. 6, which was taken with the magnetic field parallel to the c axis, has been identified as a Ta^{4+} ion. The identity of this spectrum is easily established by examining the spectrum taken with the magnetic field perpendicular to the c axis, as shown in trace (b) of Fig. 6. The spectrum splits out into an eight-line hyperfine pattern (^{181}Ta, I = 7/2, 100% abundant). The Ta^{4+} spectrum is stable at 77 K, as indicated by the x-irradiation temperature, but is difficult to observe at 77 K. However, the Ta^{4+} spectrum becomes easily observable at 17 K, where traces (a) and (b) in Fig. 6 were taken. This change in sensitivity occurs because lowering the temperature increases the population difference of the states involved in the ESR transitions. The population in the excited state, n_1, is proportional to the Boltzmann factor, that is $n_1/n_0 = \exp(-E/kT)$, where n_0 represents the population of the lower level. The population difference between the two states is responsible for an observed ESR transition, hence a decrease in the temperature, which increases the population difference, will increase the observed ESR signal.

The correlation in $LiTaO_3$ between the 470-nm optical
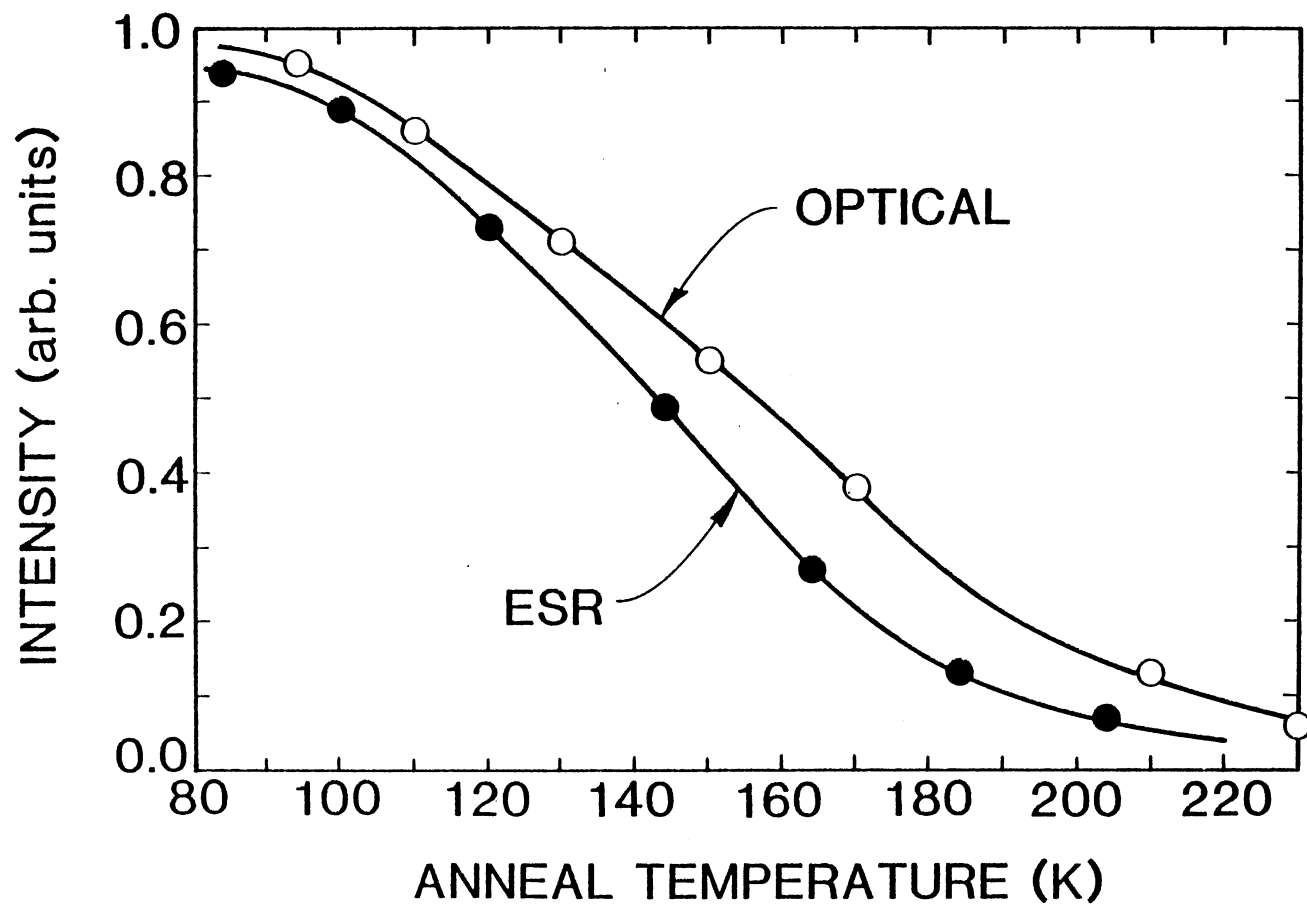
Figure 7. Thermal anneal behavior of the radiation-induced optical
absorption band and ESR hole center in LiTaO$_3$

band of Fig. 5 and the ESR hole center (at approximately 3300 gauss) of Fig. 6 is established by a pulsed thermal anneal. The experimental conditions for the anneal are the same as explained above for thermal anneals on $LiNbO_3$. Shown in Fig. 7 is the intensity of the two spectra as a function of temperature from 80 K to 230 K. The optical band and the ESR spectrum thermally decay at the same rate in the 100 K to 150 K region.

Reduction of $LiNbO_3$

In addition to x-irradiation, another method of defect production in $LiNbO_3$ and $LiTaO_3$ that was investigated is reduction. A reduction treatment involves heating the sample to temperatures above room temperature while surrounded by an atmosphere with a low oxygen partial pressure.

Impurities, such as transition-metal ions, are present in $LiNbO_3$ and $LiTaO_3$ in the part-per-million range. After $LiNbO_3$ or $LiTaO_3$ crystals are reduced, some of the impurity ions change valence state. These changes in valence can be monitored by ESR. Shown in Fig. 8 is the room temperature ESR spectra for the Fe^{3+} and Mn^{2+} ions in $LiNbO_3$ with the magnetic field parallel to the y axis of the crystal.[5-11] Trace (a) was taken on an as-received sample and shows the spectrum due to Fe^{3+}. Also observable in trace (a) are weak, six-line sets of lines due to Mn^{2+} ions. After $LiNbO_3$ is reduced in a vacuum at
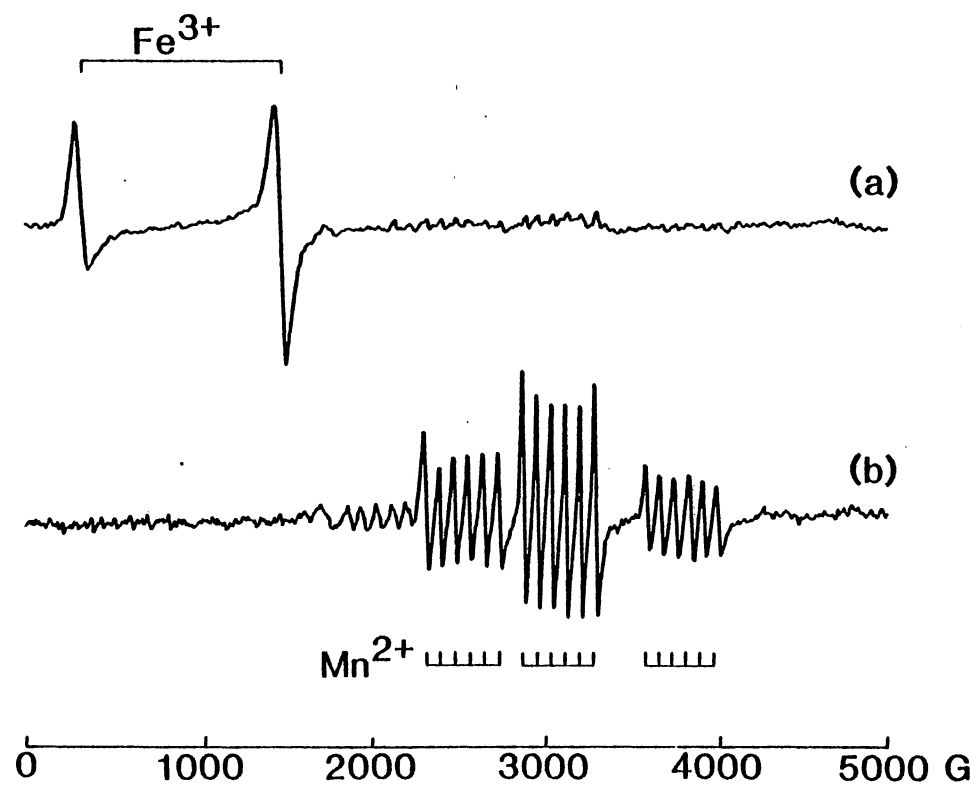
Figure 8.   ESR spectra of $LiNbO_3$ (a) before and (b) after a $1000^\circ C$ vacuum reduction
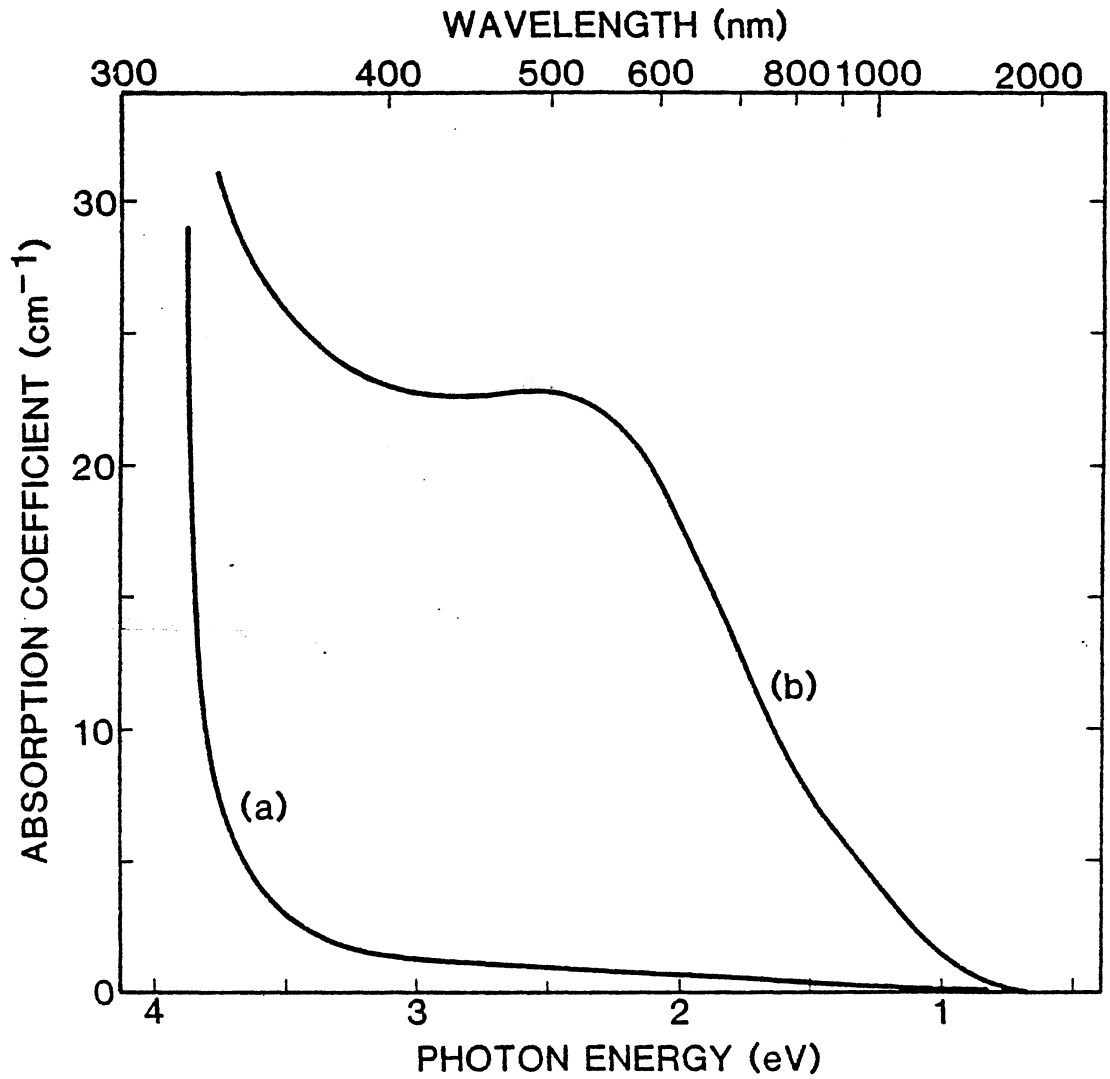
Figure 9. Optical absorption of $LiNbO_3$ (a) before and
(b) after a $1000^{\circ}C$ vacuum reduction

1000°C for 1 hour, trace (b) was obtained. The Fe^{3+} spectrum is completely eliminated and the Mn^{2+} spectrum has grown. The spectrometer's gain was the same for both traces, so that a direct comparison of the intensities can be made.

Another spectroscopic property of $LiNbO_3$ that is changed by reduction is the optical absorption. This change is presented in Fig. 9 where trace (a) is the optical absorption taken at room temperature for an as-grown $LiNbO_3$ crystal. Trace (b) of Fig. 9 was taken after a 1000°C vacuum reduction, and has a broad absorption band near 500 nm. Both traces were taken with unpolarized light propagating along the c axis. This absorption band represented by trace (b) has been assigned in the past literature to both Nb^{4+} ions[3,17] and oxygen-vacancy centers.[18-20] Our assignment for the 500-nm will be discussed at length latter in this article.

To monitor and compare these reduction-induced changes that occur in $LiNbO_3$, a single sample was heated to a desired temperature (labeled anneal temperature in Fig. 10) in a vacuum of 10^{-5} Torr and held for one hour. After cooling to room temperature, the ESR, optical absorption and infrared spectra were taken and the sequence was repeated for the next higher temperature. Results of this reducing experiment for $LiNbO_3$ are summarized in Fig. 10. The intensity of the corresponding spectral line is plotted for each of the
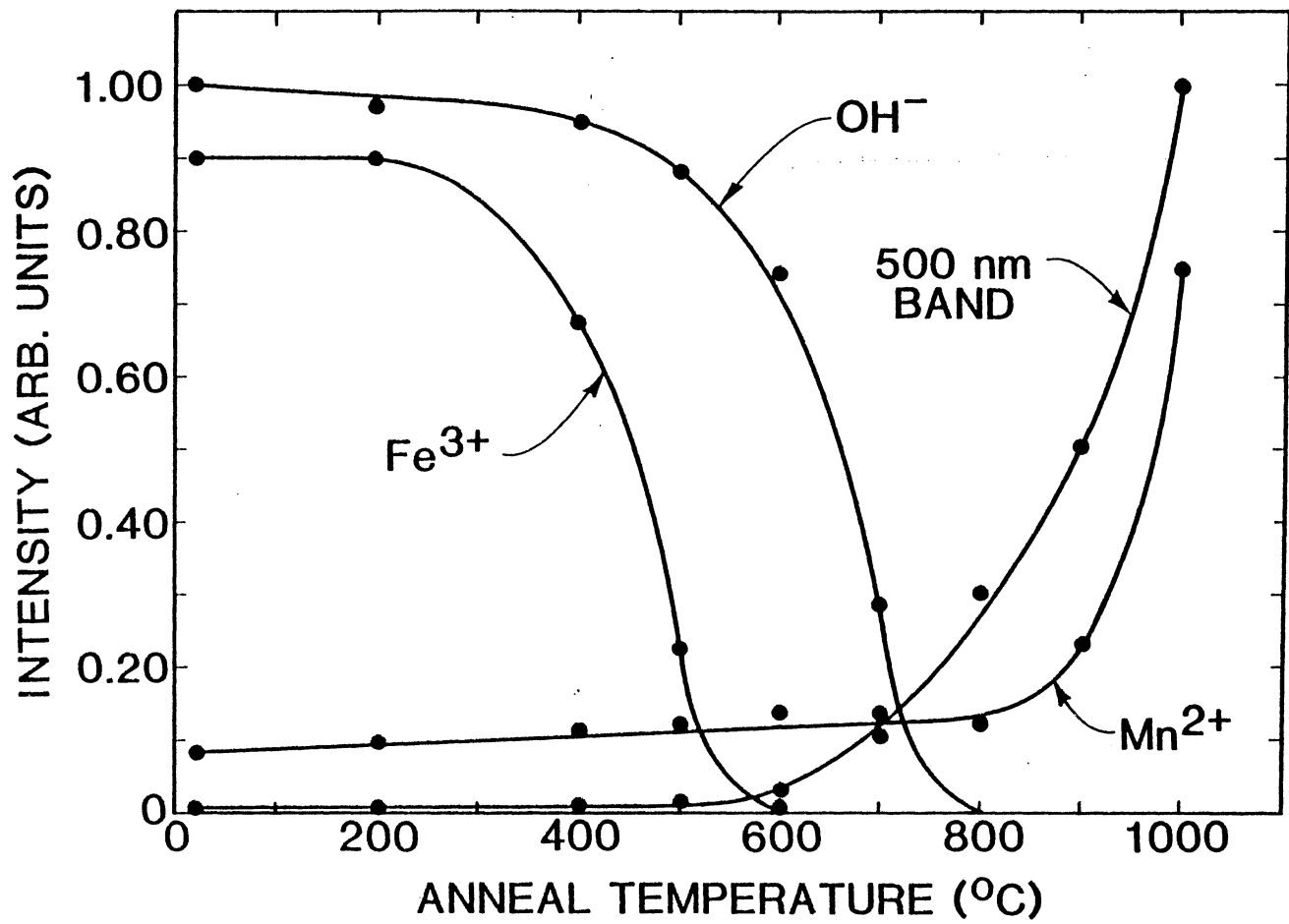
Figure 10. Results of reducing a LiNbO$_3$ crystal in a vacuum at progressively higher temperatures

four defects monitored. That is, the curve in Fig. 10 labeled "500-nm band" represents the intensity of the optical absorption peak ocurring at 500 nm and illustrated in Fig. 9. The OH^- curve represents the intensity of the infrared absorption at 3480 cm^{-1}.[21] The data in Fig. 10 were obtained from one sample, so a direct comparision of the various effects at each annealing temperature can be made. By making all measurements on the same sample, sample-to-sample variations were eliminated.

Reduction of $LiTaO_3$

Shown in Fig. 11 is the ESR spectrum for as-grown $LiTaO_3$ taken at 77 K with the magnetic field parallel to the c axis. All of the ESR lines observed are assumed to be due to transition-metal-ion impurities. For ease of discussion, the more prominent lines are labeled 1 through 6 in Fig. 11. Lines 1 and 2 are attributed to Fe^{3+} ions. This assignment is based on an analogy with $LiNbO_3$ where Fe^{3+} has been shown to have transitions in the same field region as lines 1 and 2.[22] Line 4 is assigned to Cr^{3+} on the basis of work by Burns et al.[23], and lines 3, 5, and 6 have not been identified.

To compare the effects of reduction with those summarized in Fig. 10 for $LiNbO_3$, the same reduction experiment was conducted on $LiTaO_3$. Fig. 12 illustrates the changes in intensity for the ESR lines of Fig. 11 as

LiTaO$_3$

H ∥ c axis

77 K

1 2

3 5 6

4

0   1000   2000   3000   4000   5000 G
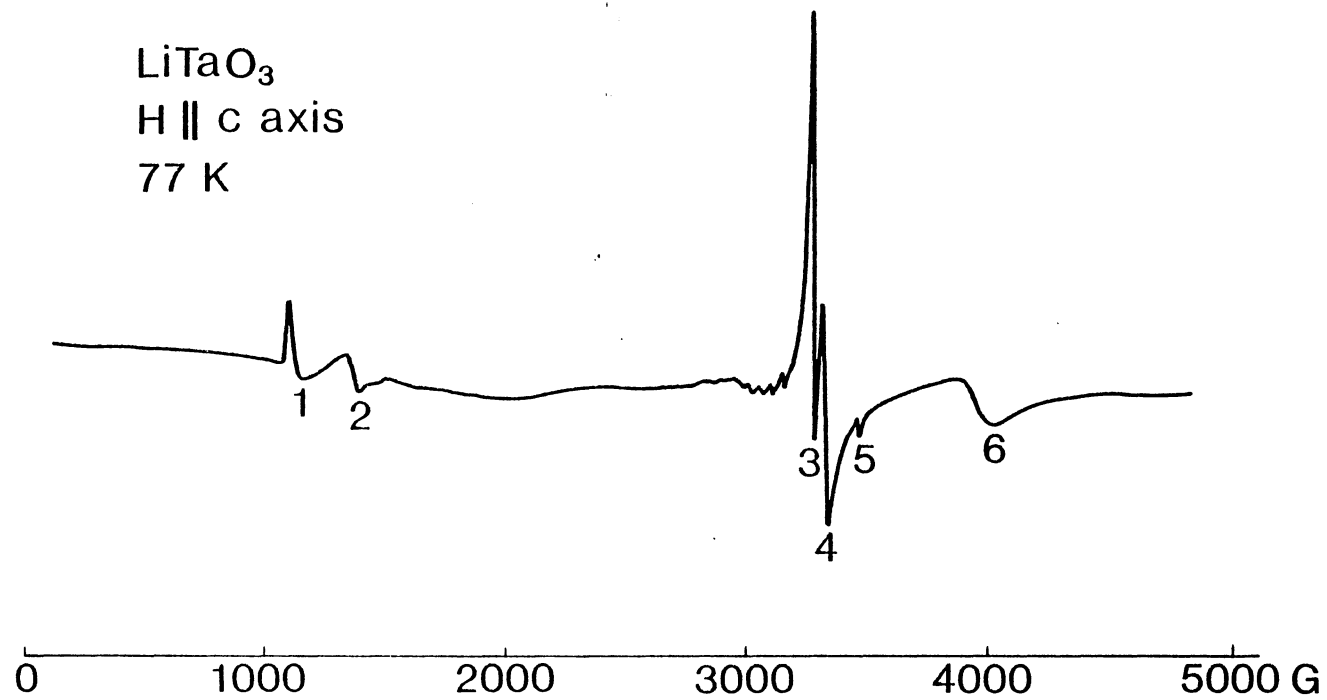
Figure 11.   ESR spectrum of as-grown LiTaO$_3$ taken at 77 K
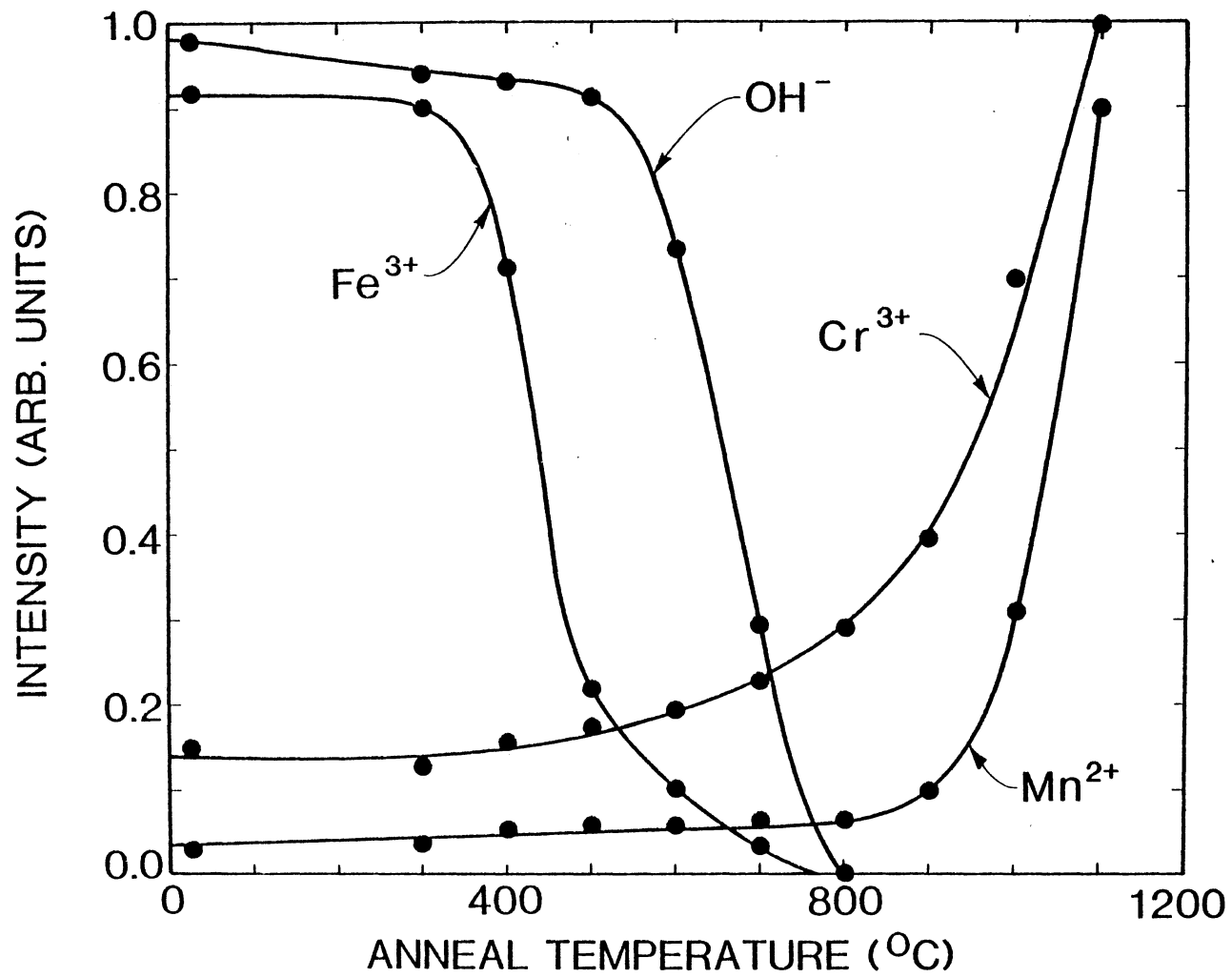
Figure 12. Results of reducing a LiTaO$_3$ crystal in a vacuum at progressively higher temperatures
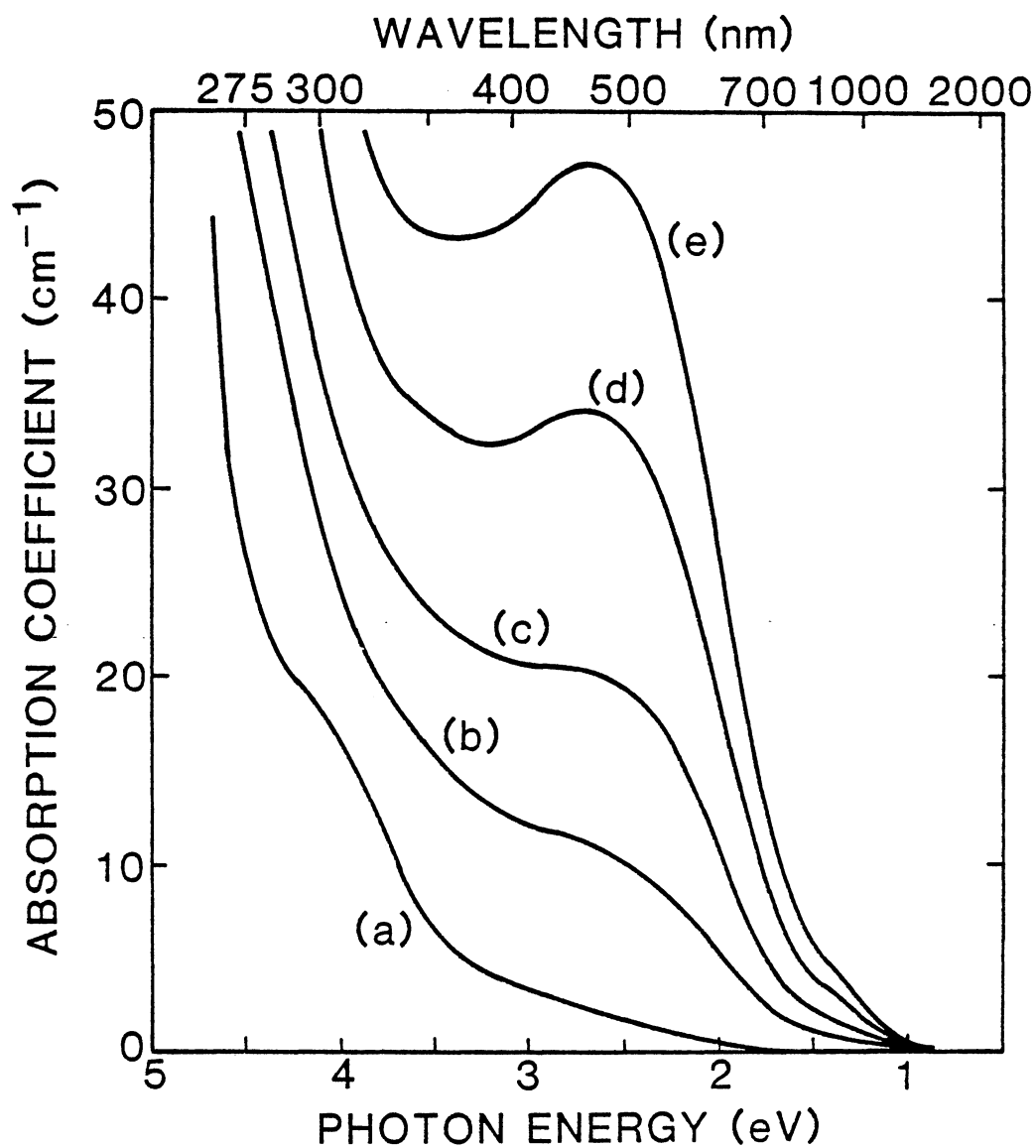
Figure 13. Optical absorption of LiTaO₃ (a) before
and after a series of argon reductions
at (b) 850°C, (c) 875°C, (d) 900°C,
and (e) 925°C

the LiTaO$_3$ sample is reduced at progressively higher temperatures. The experimental conditions are the same as those detailed for Fig. 10 on LiNbO$_3$ in the previous section. The infrared absorption intensity plotted in Fig. 12 is also at 3480 cm^{-1}, as in LiNbO$_3$. The important feature of this vacuum reduction experiment on LiTaO$_3$ is the failure to induce any significant visible coloration of LiTaO$_3$ for the temperatures up to 1100°C.

Two factors which influence the reduction are temperature and oxygen partial pressure. The temperature and oxygen partial pressure that induced the 500-nm band in LiNbO$_3$, shown in Fig. 9, were insufficient to produce a significant optical band in LiTaO$_3$. The maximum temperature was limited by the availiable furnace, and the only other option was to decrease the oxygen partial pressure in the reducing atmosphere. Thus, LiTaO$_3$ was reduced in an argon atmosphere contained in a stainless steel tube. This argon reduction produced a 470-nm optical band in LiTaO$_3$, as shown in Fig. 13. Curve (a) represents the initial absorption in the as-grown LiTaO$_3$ crystal. Curves (b), (c), (d), and (e) show the absorption after the crystal was held in an argon atmosphere for one hour at 850°C, 875°C, 900°C, and 925°C, respectively. The absorption measurements were made at 85 K using unpolarized light propagating along a direction perpendicular to the c axis of the sample. Figure 13 illustrates the growth of this 470-nm optical

band as the reducing temperature is increased.

F to F^+ Conversion in $LiNbO_3$ and $LiTaO_3$

In this section, results will be presented on a major class of defects in $LiNbO_3$ and $LiTaO_3$ which are induced by reduction. After $LiNbO_3$ has been reduced at $1000^\circ C$ in a vacuum, a 500-nm optical absorption band is present, as shown in trace (b) of Fig. 9. The growth of this 500-nm band with vacuum-anneal temperature is plotted in Fig. 10. A similar behavior is observed in $LiTaO_3$ after a high-temperature argon reduction. Fig. 13 shows the growth of the reduction-induced 470-nm band. Thus, in both $LiNbO_3$ and $LiTaO_3$, defects produced by reduction give rise to optical absorption bands having similar band shapes and peaking near the same energy. These similarities in isomorphic crystals suggest the same defect is present in both materials.

Reproduced in trace (b) of Fig. 14, is the 500-nm optical absorption band of $LiNbO_3$ taken at 80 K after a reduction at $900^\circ C$ for 1 hour. The data in Fig. 14 was taken with unpolarized light propagating along the c axis of the sample. After the sample is bleached at 80 K with the unfiltered output of a 150-W xenon lamp, the optical absorption is changed and is shown in trace (c) of Fig. 14. The initial 500-nm band of trace (b) decreases and a band near 760 nm increases. This optically induced 760-nm band is only stable at low temperatures, i.e., the
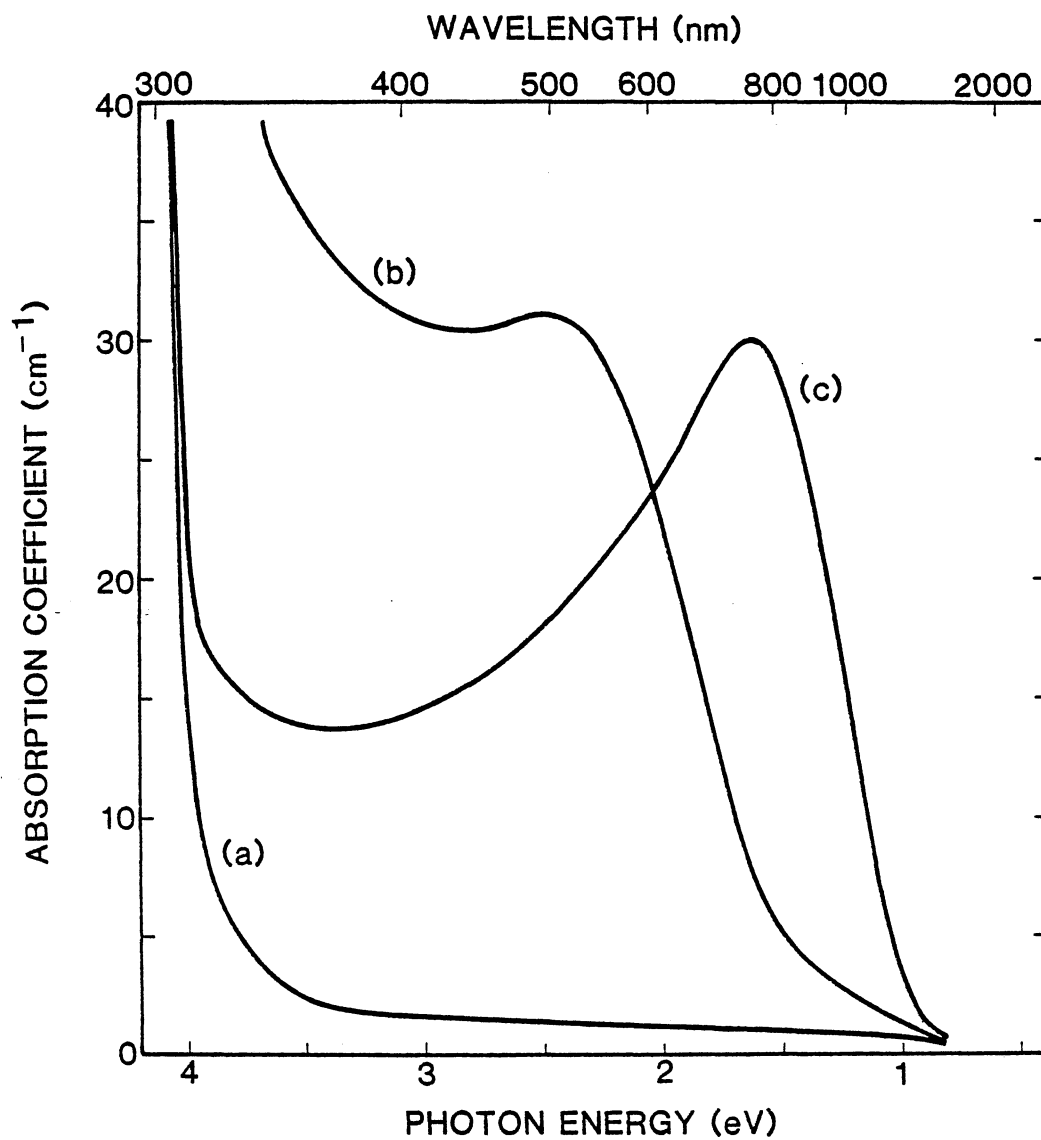
Figure 14. Optical absorption of $LiNbO_3$ at 77 K. Trace
(a) is as-grown, trace (b) is after a
$1000^\circ C$ vacuum reduction, and trace (c) is
after the reduced sample was bleached with
a xenon lamp
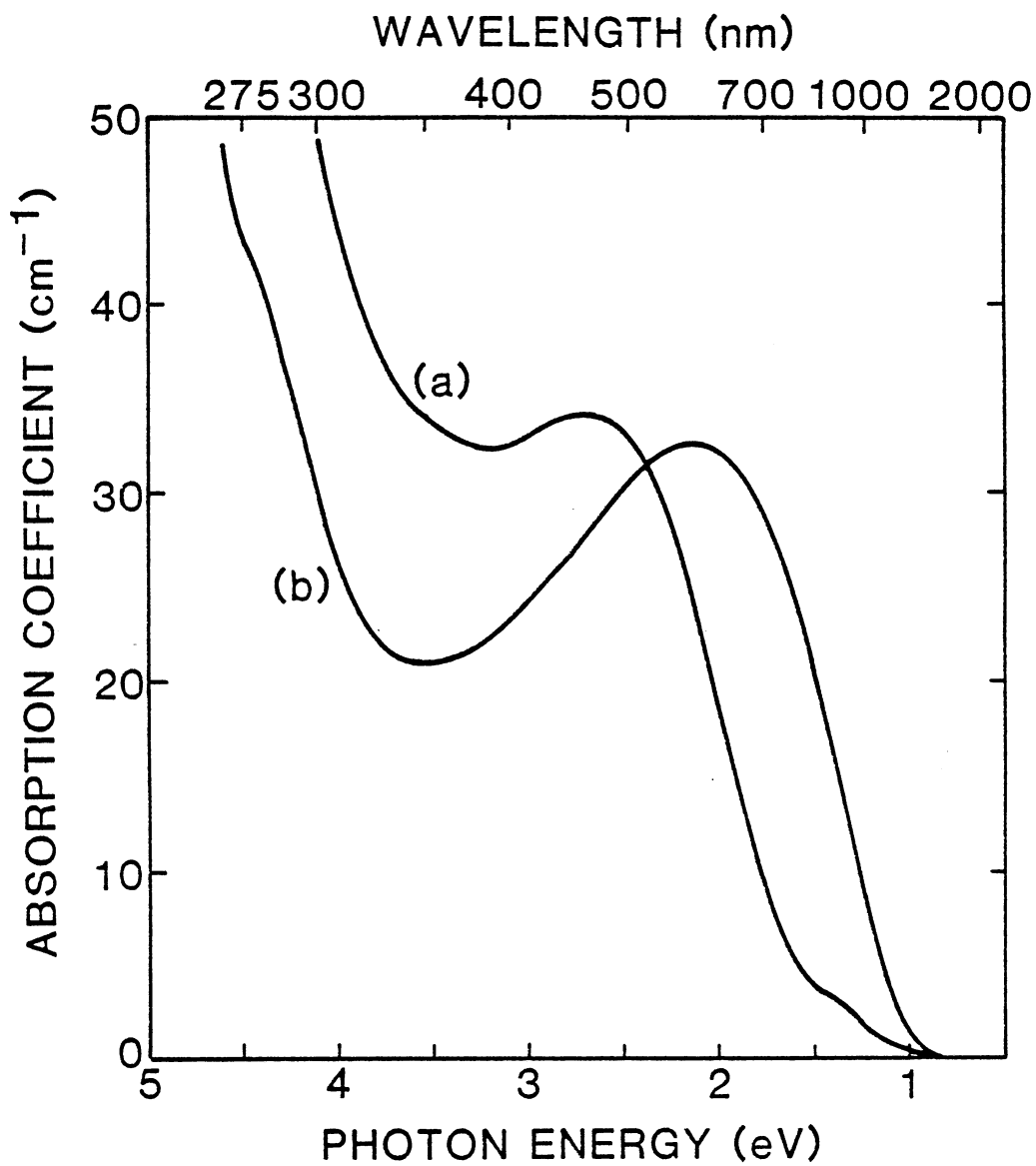
Figure 15. Trace (a) is the optical absorption of
LiTaO$_3$ after a 900°C argon reduction
and trace (b) is after the reduced
sample was bleached with a xenon lamp

500-nm band of trace (b) is restored by warming the sample to room temperature.

The same optical conversion that was illustrated in Fig. 14 for $LiNbO_3$ is shown in Fig. 15 for $LiTaO_3$. Trace (a) of Fig. 15 (reproduced from trace (d) of Fig. 13) is the absorption at 85 K of $LiTaO_3$ after a 900^oC argon reduction. The data in Fig. 15 was taken with unpolarized light propagating along a direction perpendicular to the c axis. After bleaching at 85 K with a xenon lamp, the 470-nm band of trace (a) disappears and a 570-nm band increases. As with $LiNbO_3$, the conversion in $LiTaO_3$ is only stable at low temperatures.

The spectral dependence of the light needed to convert the 500-nm band to the 760-nm band in $LiNbO_3$ was investigated. A measure of the optical conversion that occured during the bleach is the change in the absorption coefficient at 800 nm. That is, the difference in the absorption coefficient between trace (c) and trace (b) of Fig. 14. Using a monochromator (2.5-mm slit width) and a long-pass 310-nm glass filter, this difference in absorption coefficient at 800 nm was measured after a 5-minute bleach at a particular wavelength. The sample was warmed to room temperature after each measurement to reconvert back to the 500-nm band. The results of this study are plotted in Fig. 16 by the dashed curve. Also shown in Fig. 16 is the 500-nm absorption band for
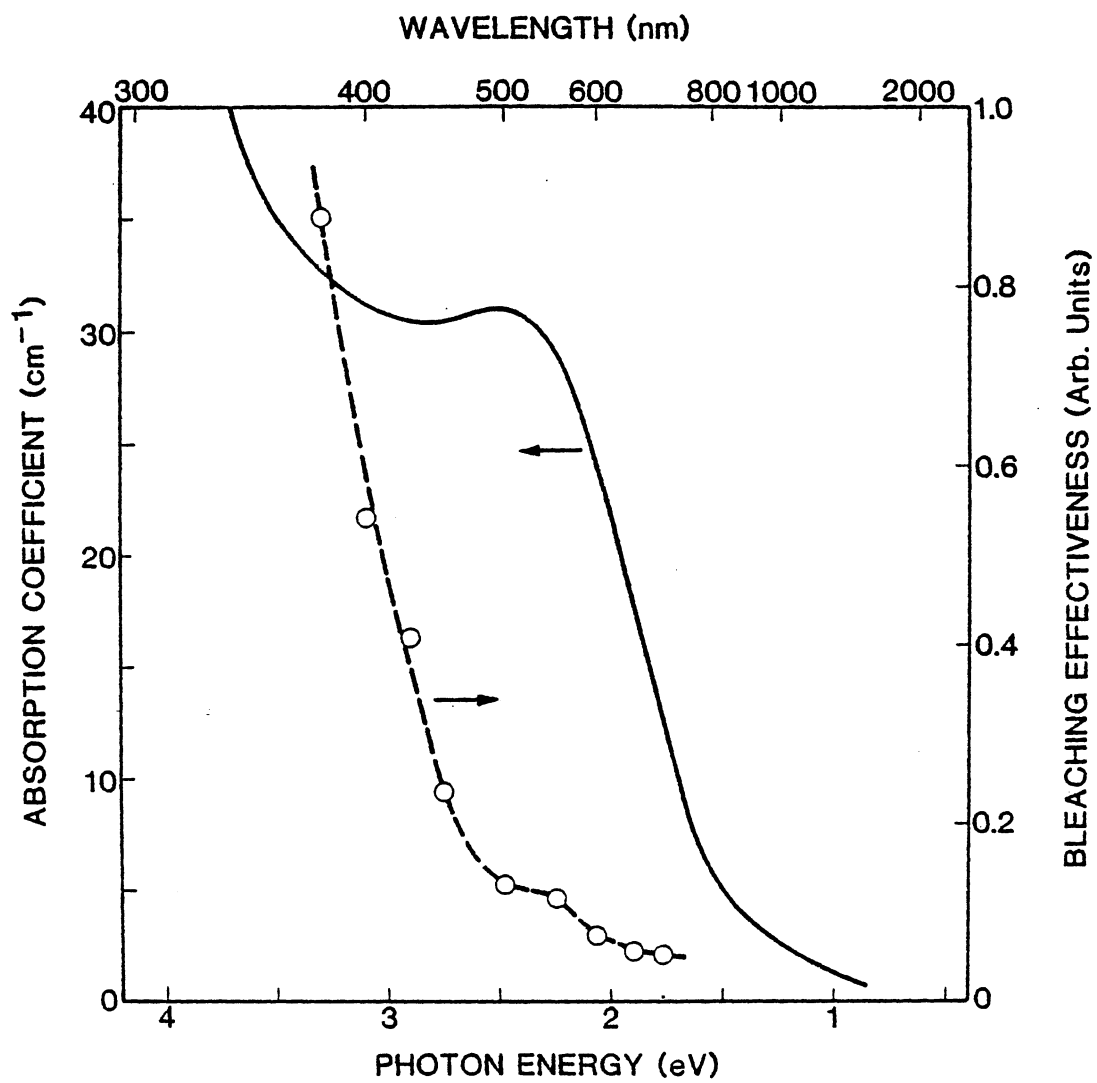
Figure 16. Spectral dependence of the bleaching light needed to convert the 500-nm band (solid curve) to the 760-nm band in reduced LiNbO$_3$

comparison.

ESR data corresponding to the optical conversion in LiNbO$_3$ is illustrated in Fig. 17. Trace (a) in Fig. 17 is the ESR spectrum taken at 77 K after the sample was reduced in a vacuum at 900°C. Thus, trace (a) in Fig. 17 and trace (b) in Fig. 14 represent the ESR and optical absorption of LiNbO$_3$ after a reduction. Trace (b) in Fig. 17, taken at 77 K, is the ESR spectrum after a 77 K bleach by a xenon lamp. The optical bleach causes a Nb^{4+} ESR spectrum to increase. This Nb^{4+} spectrum anneals when the sample is warmed to room temperature. Thus, trace (b) of Fig. 17 and trace (c) of Fig. 14 correspond to reduced LiNbO$_3$ after the low-temperature bleaching. That is, a low-temperature bleach in reduced LiNbO$_3$ induces a 760-nm optical absorption and a Nb^{4+} ESR spectrum.

To establish a correlation between the 500-nm band in LiNbO$_3$ and the Nb^{4+} ESR spectrum formed by bleaching, the intensity of each was plotted as a function of the reduction temperature. This is shown in Fig. 18, where the open circles represent the intensity of the 500-nm absorption band and the filled circles represent the intensity of the Nb^{4+} ESR spectrum formed by the optical conversion at 77 K. After a specific reduction, the intensity of the 500-nm band and the intensity of the Nb^{4+} ESR spectrum formed by bleaching was measured, and the cycle was repeated at the next higher reduction
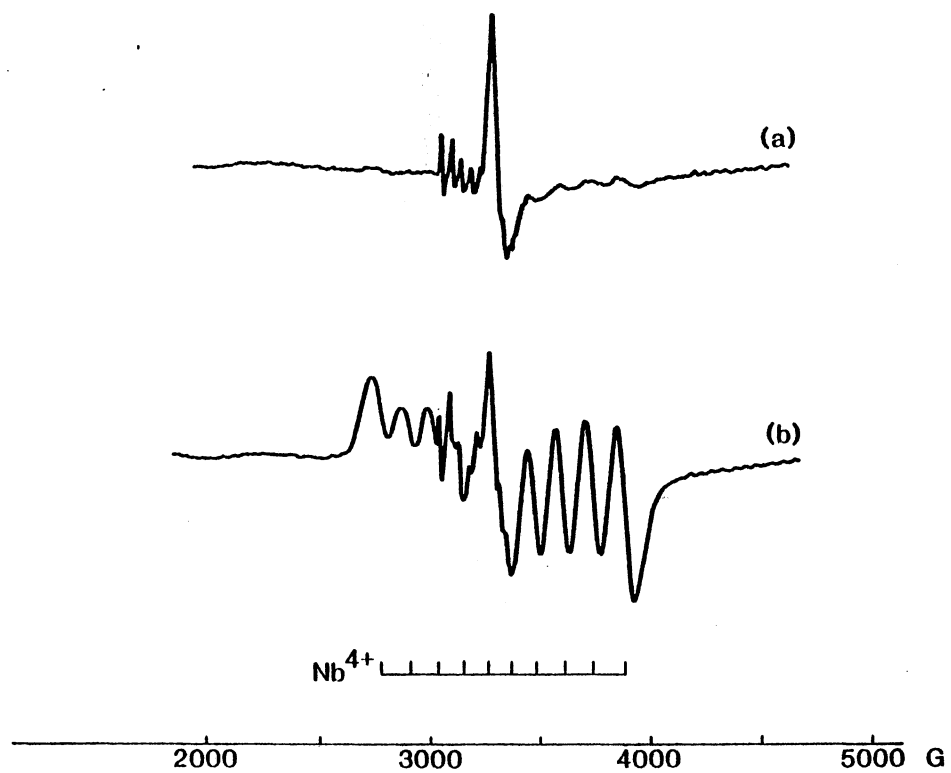
Figure 17. ESR spectra of LiNbO$_3$ after a 1000°C vacuum reduction. Trace (a) is before and trace (b) was taken after an optical bleach at 77 K
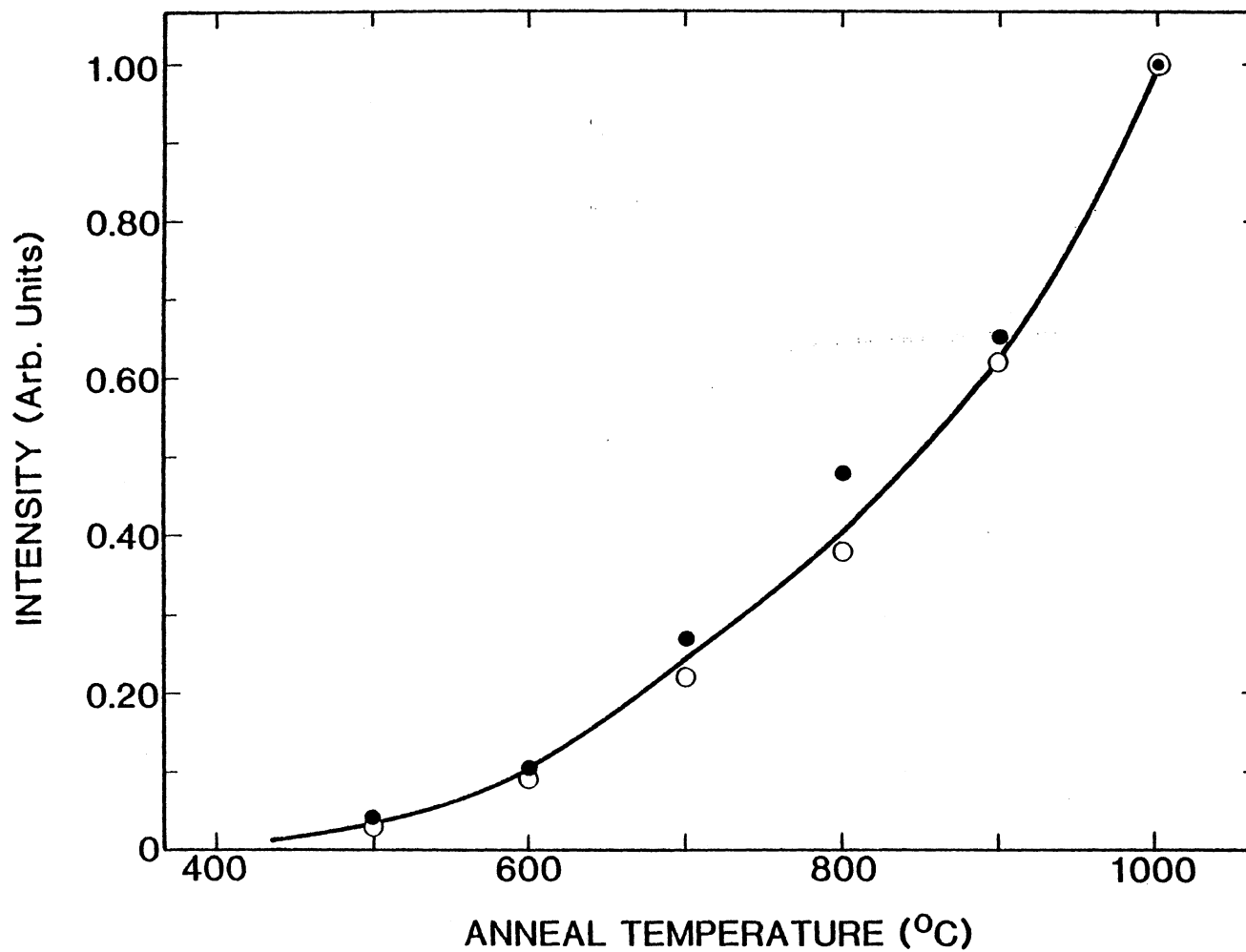
Figure 18. Correlation between the intensity of the F center absorption band (open circles) and the intensity of the Nb^{4+} ESR spectrum formed by bleaching light (filled circles) in $LiNbO_3$
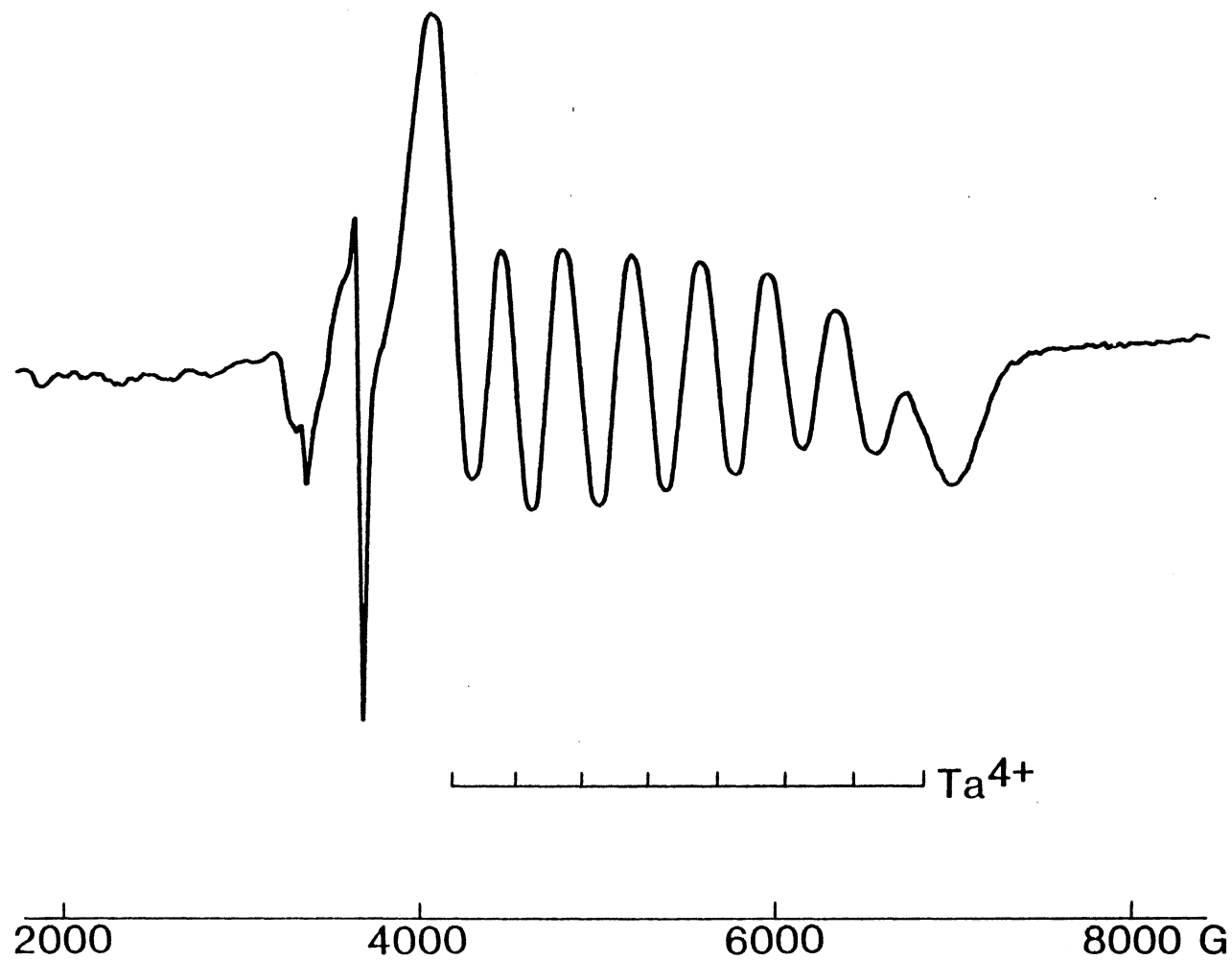
Figure 19. ESR spectrum of reduced $LiTaO_3$ at 17 K after an optical bleach
at 17 K with a xenon lamp

temperature. Thus, a correlation exists between the 500-nm band induced by reduction and the intensity of the Nb^{4+} ESR spectrum that can be formed by optical conversion at 77 K.

In analogy to $LiNbO_3$, ESR data for the optically-induced conversion in $LiTaO_3$ is shown in Fig. 19. After a $900^{\circ}C$ argon reduction, $LiTaO_3$ was bleached at 14 K with a xenon lamp and the spectrum in Fig. 19 was taken at 14 K with the magnetic field perpendicular to the c axis of the sample. An eight-line hyperfine pattern, not present before the bleach, is shown in Fig. 19. The hyperfine pattern is due to the ^{181}Ta (I = 7/2, 100% abundant) nuclei. The growth of this eight-line hyperfine pattern takes place in conjunction with the optical-absorption conversion for $LiTaO_3$ that was illustrated in Fig. 15.

These results establish a very similar pattern between the optical absorption and ESR spectra of reduced $LiNbO_3$ and $LiTaO_3$. The identity of the 500-nm band in reduced $LiNbO_3$ and the 470-nm band in reduced $LiTaO_3$ is a crucial first step in understanding the major defects in these materials. Two different possibilities for the assignment of the 500-nm band in reduced $LiNbO_3$ have been suggested in the literature; these are Nb^{4+} ions[3,17] and oxygen-vacancy centers[18-20,24,25]. The data presented in this dissertation points out two inconsistencies with the assignment of the 500-nm band to Nb^{4+} absorption. The first of these is the temperature

stability of the 500-nm band and the Nb^{4+} ESR spectrum are not the same. The Nb^{4+} spectrum induced by a low-temperature bleach is not stable at room temperature, whereas the 500-nm band is. Also, the intensity of the Nb^{4+} ESR pattern increases and the intensity of the 500-nm band decreases when the reduced $LiNbO_3$ crystals are optically bleached at low temperature. Thus Nb^{4+} is not a reasonable defect assignment for the 500-nm band in $LiNbO_3$.

Another important point in establishing the identity of the 500-nm band in $LiNbO_3$ and the 470-nm band in $LiTaO_3$ is that the introduction of these bands takes place only in an oxygen-deficient atmosphere and the bands will decrease if the sample is oxidized (i.e., heated in an oxygen atmosphere). Thus, the 500-nm absorption band can be cycled and the key ingredient is the oxygen partial pressure in the surrounding atmosphere during the heat treatment. This correlation with oxygen strongly suggests that the reasonable candidate for the identity of the reduction-induced optical bands in $LiNbO_3$ and $LiTaO_3$ is an oxygen-vacancy center. During heat treatments, oxygen ions can diffuse out of the crystal. The oxygen vacancies formed during reduction would be neutrally charged when they contain two electrons, thus the 500-nm band in $LiNbO_3$ and the 470-nm band in $LiTaO_3$ (i.e., the most stable configuration for the defect) are assigned to oxygen vacancies with two electrons. These

two-electron vacancies are known as F centers. The photoconversion at 77 K removes one of these electrons from the vacancy and this electron is trapped at a Nb^{5+} ion or a Ta^{5+} ion, thus forming the Nb^{4+} or the Ta^{4+} observed by ESR. The existence of F and F^+ centers in other oxides such as MgO, CaO, SrO,[26] and Al_2O_3[27] has been firmly established, hence it is not unreasonable to expect oxygen vacancies in $LiNbO_3$ and $LiTaO_3$ also.

After the optical conversion at 77 K, the sample contains both F^+ centers (oxygen vacancies with one electron) and an electron trapped on either a Nb^{5+} or Ta^{5+} ion. Both the F^+ center and the cation contain an unpaired spin and each should give rise to an ESR signal. Only the broad hyperfine pattern is observed in Fig. 17 (Nb^{4+}) and Fig. 19 (Ta^{4+}), thus accounting just for the electron trapped at the cation. This absence of an observable ESR signal for the F^+ center can be interpreted as follows: the F^+ spectrum is broadened by hyperfine interactions with the surrounding ions (^{93}Nb, ^{181}Ta, ^{6}Li, ^{7}Li) and has no resolved structure. Such a broad ESR spectrum would be very difficult to detect. It is not unreasonable to expect that an electron trapped at an oxygen vacancy would be delocalized onto the surrounding ions in the covalent materials $LiNbO_3$ and $LiTaO_3$. That the ESR spectrum of the F^+ center in $LiNbO_3$ should be very broad, and thus difficult to detect, is supported by results in Al_2O_3.[28]

After making the assignment of the 500-nm optical band in LiNbO$_3$ and the 470-nm optical band in LiTaO$_3$ to F centers, the question arises as to the identity of the optical absorption after the low temperature conversion, which is illustrated in trace (c) of Fig. 14 for LiNbO$_3$ and trace (b) of Fig. 15 for LiTaO$_3$. The absorption after photoconversion should be composed of F$^+$ center absorption and either Nb^{4+} or Ta^{4+} absorption. The absence of two resolved bands in either trace (c) of Fig. 14 or trace (b) of Fig. 15 makes an assignment difficult.

The σ-polarized optical absorption data for x-irradiated LiNbO$_3$ shown in Fig. 2 peaks near 500 nm and has a shoulder near 800 nm which is not present in the π-polarized absorption. The ESR spectrum after the irradiation consists of a hole center and a Nb^{4+} ten-line hyperfine pattern. The hole center has been assigned to the 500-nm band[3] in analogy with trapped hole center absorption in other oxide materials.[26] The presence of the 800-nm shoulder suggests that Nb^{4+} could have a σ-polarized absorption band in this region. After the low-temperature photoconversion of reduced LiNbO$_3$, an optical absorption band is expected for both F$^+$ centers and Nb^{4+} ions. If the Nb^{4+} is assigned to the σ-polarized absorption near 800 nm, as suggested from the x-irradiation data, then this assignment suggests that the main contribution (σ polarization) to trace (c) of Fig. 14 is absorption by Nb^{4+}. Then a possibility for the F$^+$

center absorption is in the high energy tail in trace (c) of Fig. 14. If the F^+ center has absorption in this region, then this implies a significant difference in the oscillator strengths for the F^+ and the F band (500-nm band).

The other possibility is to assign the 760-nm band of trace (c) in Fig. 14 to F^+ centers. This implies that the oscillator strengths of the F and F^+ centers will be comparable as has been demonstrated in other oxides such as MgO, CaO, and Al_2O_3.[26] With the F^+ center assigned to the 760-nm band, there is no obvious absorption for Nb^{4+}. A problem with the assignment of the 760-nm band to F^+ centers in $LiNbO_3$ is the shoulder near 800 nm after the 77- K x-irradiation.[29] If this 800-nm shoulder is also interpreted as F^+ center absorption, then to reconcile the observation of F^+ centers after an irradiation requires either a significant oxygen vacancy concentration in an as-grown crystal or oxygen vacancy production during irradiation. A 500-nm band, representing two-electron oxygen vacancies, of sufficient intensity does not seem to be present in the as-grown crystals. The literature on x-ray-induced defect production in oxides does not support the possibility of oxygen vacancies being produced by x-irradiation.[26] Thus, the assignment of the 760-nm band in $LiNbO_3$ to F^+ centers has not been firmly established.

The absorption for x-irradiated $LiTaO_3$, as shown in
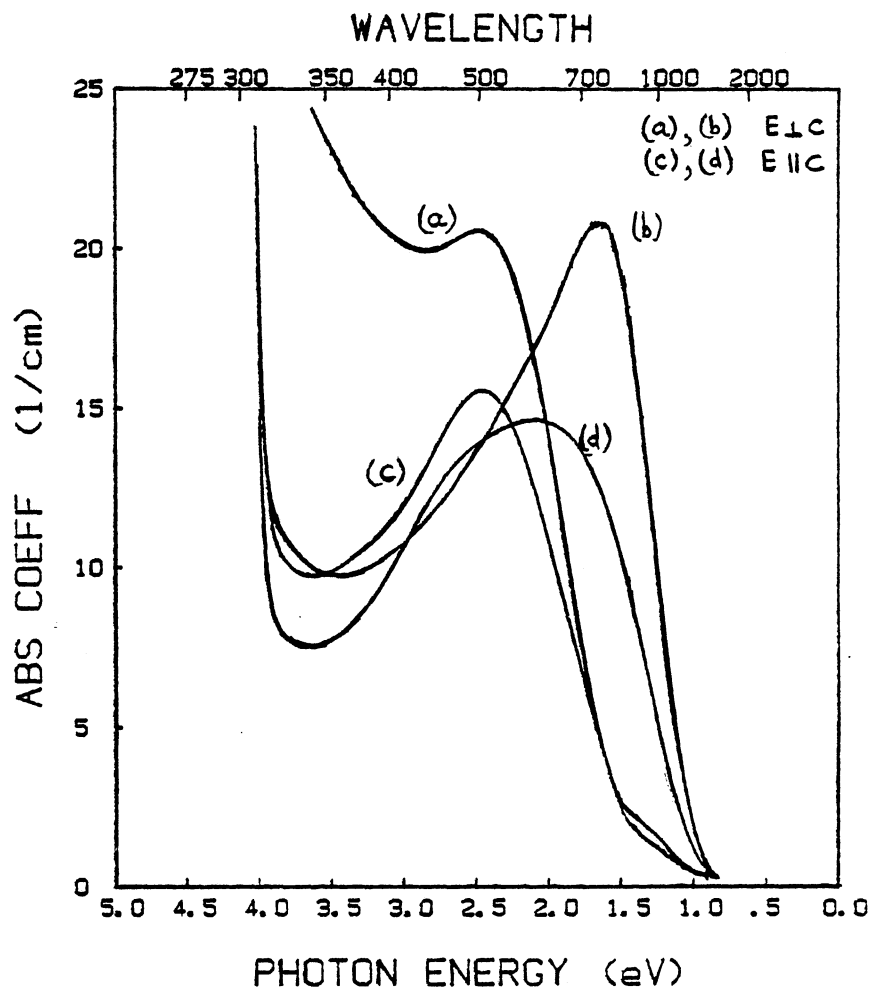
Figure 20. Polarized optical absorption for
reduced LiNbO$_3$ at 85 K before
and after an optical bleach
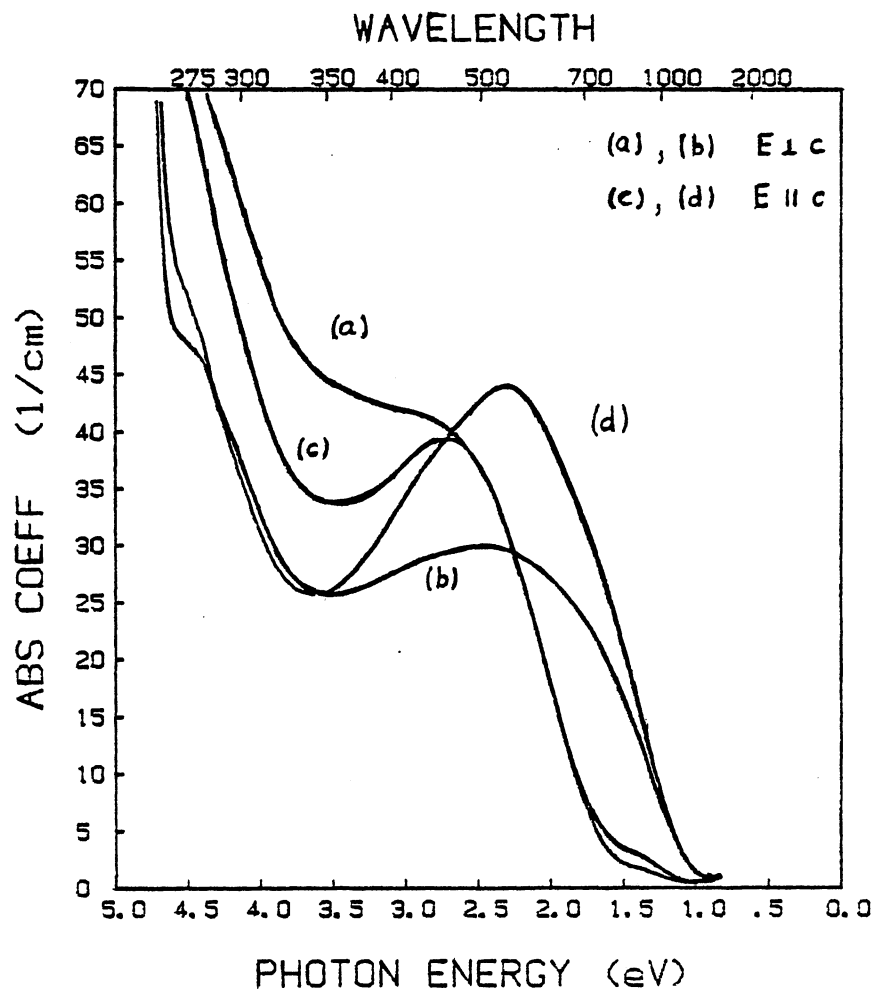
Figure 21. Polarized optical absorption for reduced LiTaO₃ at 85 K before and after an optical bleach

Fig. 5, also shows a slight side band at approximately

1.4 eV. In analogy to $LiNbO_3$, a possibility exists that

this 1.4 eV band represents Ta^{4+} absorption. To examine

this possibility, polarized optical absorption for

reduced $LiNbO_3$ and $LiTaO_3$ is shown in Figures 20 and 21,

respectively. Each figure shows both polarizations

before and after the 77-K photoconversion. A direct

analogy does not seem to exist between the two materials.

In particular, the 1.4 eV σ-polarized band present after

x-irradiation in $LiTaO_3$ is not pronounced in the

photoconverted $LiTaO_3$ spectrum (trace (b) in Fig. 21).

Angular Dependence of Ta^{4+} in $LiTaO_3$

The ESR spectra for the Ta^{4+} hyperfine pattern in

$LiTaO_3$ are shown in Fig. 22. The spectra were obtained

after $LiTaO_3$ was reduced in argon at $925^{\circ}C$ for one hour.

Following the reduction, the sample was cooled to 17 K

and then illuminated with a xenon lamp to produce the ESR

pattern observed. An interesting feature of the Ta^{4+}

spectrum is demonstrated by observing the pattern with

the magnetic field, H, parallel and perpendicular to the

c axis of the crystal. Trace (b) in Fig. 22, with H

perpendicular to the c axis, shows the eight-line

hyperfine pattern due to the ^{181}Ta (I = 7/2, 100%

abundant) nucleus. Rotation of the sample to H parallel

to the c axis shows that the Ta^{4+} spectrum, indicated by

an arrow in trace (a) of Fig. 22, has collapsed and moved
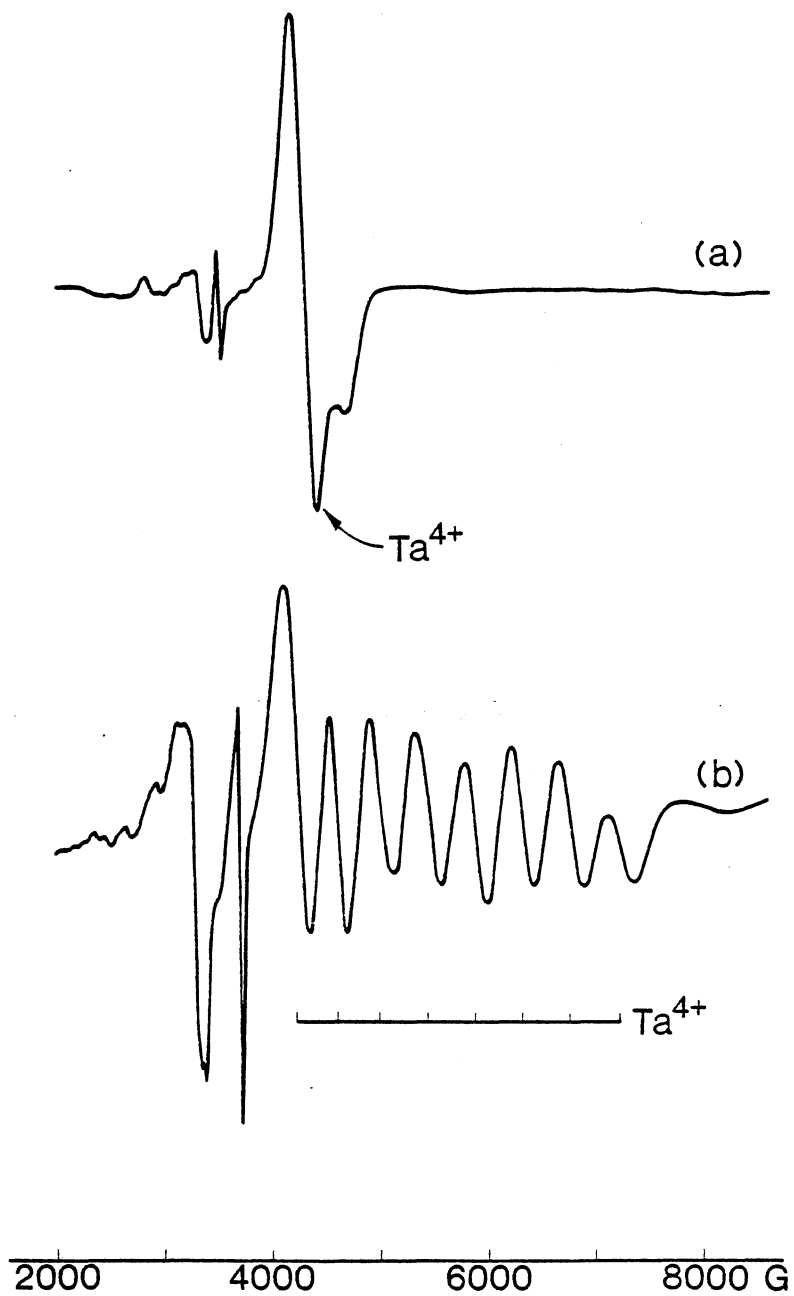
Figure 22. ESR spectra of Ta^{4+} in reduced LiTaO$_3$
at 17 K. Trace (a) is parallel and
trace (b) is perpendicular to the
crystal's c axis

down field. A detailed angular dependence analysis of
this Ta^{4+} ESR spectrum was made. The magnetic field
positions of the ESR lines were fitted to the spin-
Hamiltonian

$$H = B_e \vec{H} \cdot \overleftrightarrow{g} \cdot \vec{S} + \vec{S} \cdot \overleftrightarrow{A} \cdot \vec{I} - g_n \, B_n \, \vec{H} \cdot \vec{I}$$

for an $S = 1/2$, $I = 7/2$ spin system. The first term
describes the interaction of the spin S with the magnetic
field H, the second term treats the interaction between S
and the nuclear spin I, while the last term takes into
account the effect of H on the nuclear spin I.

The angular dependence data of Ta^{4+} was obtained every
15° for a rotation of the magnetic field in the x - y
plane and in the c - y plane of the crystal. Analysis of
the data for the x - y plane showed that within
experimental error the spectrum is axially symmetric with
respect to the c axis. The magnetic field positions of
the Ta^{4+} spectrum are tabulated in Table I as a function
of the angle between the c axis and the magnetic field.
A complete set of data was not possible at the smaller
angles because each of the lines is very broad and as the
spectrum collapsed the line positions were no longer
resolvable.

The angular dependence of the Ta^{4+} spectrum for
rotations of the magnetic field H in the crystal's c - y
plane is shown in Fig. 23. Experimental data points are
plotted in the figure. As can be seen, the spectrum

TABLE I

ESR DATA FOR THE ANGULAR DEPENDENCE OF THE
Ta^{4+} CENTER IN $LiTaO_3$

ANGLE (MEASURED FROM C AXIS)	MAGNETIC FIELD IN GAUSS	MICROWAVE FREQUENCY IN GHz
+90°	4232.2	9.45918
	4604.5	
	4984.6	
	5458.1	
	5889.2	
	6321.8	
	6766.7	
	7221.1	
+75°	4217.9	9.46041
	4586.9	
	4956.0	
	5362.7	
	5763.5	
	6173.4	
	6585.4	
	7031.8	
+60°	4168.6	9.46067
	4501.1	
	4806.5	
	5143.2	
	5477.2	
	5803.3	
	6135.2	
	6466.1	
+45°	–	9.46169
	4380.2	
	4595.0	
	4831.9	
	5073.7	
	5315.5	
	–	
	–	

TABLE I (continued)

ANGLE (MEASURED FROM THE C AXIS)	MAGNETIC FIELD IN GAUSS	MICROWAVE FREQUENCY IN GHz
-45°	– 4299.0 4512.2 4741.3 4957.6 5167.6 – –	9.46361
-60°	4128.8 4429.5 4731.7 5037.1 5345.7 5657.5 5958.1 6268.3	9.46389
-75°	4194.1 4540.8 4898.7 5307.5 5692.5 6083.8 6476.7 6875.9	9.46393
-90°	4229.1 4601.3 4986.2 5445.9 5884.9 6314.4 6763.0 7225.9	9.46409

LITHIUM TANTALATE
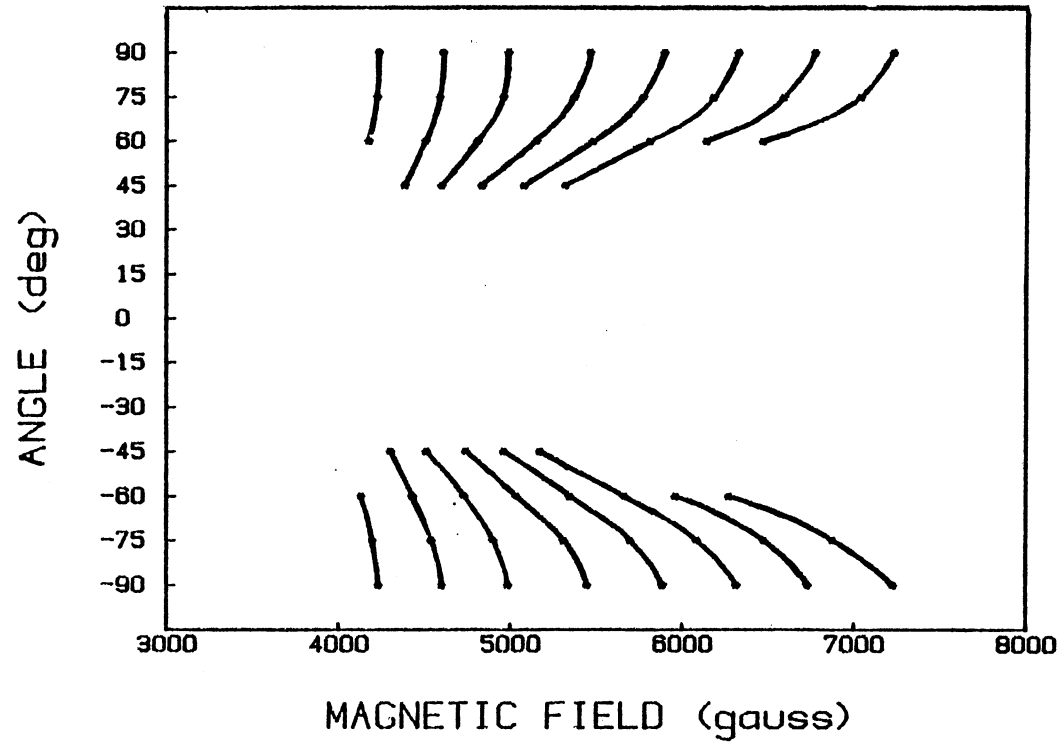
Figure 23.   Angular dependence of Ta^{4+} in $LiTaO_3$ for
             rotations of the magnetic field in the
             c - y plane with the angle measured from
             the c axis

collapses as the crystal is rotated in the c - y plane. The data points were fitted to the axially symmetric Hamiltonian and the four parameters were determined to be g_x (=g_y) = 1.17, g_z = 1.47, A_x (=A_y) = 702 MHz, and A_z = 70 MHz. Using these parameters, the experimental line positions at all angles can be calculated and these angular dependence curves (solid lines) are plotted with the experimental data points in Fig. 23.

This angular dependence analysis contains two important points about the defect structure of Ta^{4+}. After reduction, $LiTaO_3$ contains oxygen vacancies with two electrons. The low temperature bleach produces the eight-line hyperfine pattern analyzed above. After bleaching, one electron is excited out of the vacancy, leaving an F^+ center, and the other electron is trapped elsewhere in the crystal. Two ESR spectra are expected after the bleach, one for the F^+ center and another for the trapped electron. Since only one ESR spectrum is observed, the question arises as to which defect the ESR spectrum represents. An F^+ center electron could be delocalized onto the neighboring tantalum nucleus, thus giving rise to a hyperfine pattern. This possibility is ruled out because the observed Ta^{4+} ESR spectrum is axially symmetric about the c axis, and an F^+ center electron interacting with a tantalum would not have a spectrum that is symmetric about the c axis.

A self-trapped electron on a tantalum ion would have

an axially symmetric spectrum as is observed. This
assignment of a self-trapped electron on a tantalum still
leaves open the question of its exact site in the
crystal. The tantalum that traps the electron could
either be on a tantalum site or on a lithium site. The
tantalum on a lithium site, or "antisite" tantalum, was
proposed by Nassau and Lines[12] to account for the large
deviations from stoichiometry observed in lithium niobate
and lithium tantalate.

Another important point obtained from this analysis
of the angular dependence of the Ta^{4+} ESR spectrum is
information about the spatial direction of the Ta^{4+} 5d
electron. The hyperfine tensor, $\overleftrightarrow{A}$, is anisotropic and
gives rise to the strong angular variation observed
within the hyperfine pattern. The origin of the
anisotropic behavior is a dipole-dipole interaction
between the magnetic moment of the electron and the
magnetic moment of the tantalum nucleus. The hyperfine
splitting is given by an expression of the form

$$H = A + B(3\cos^2\theta - 1)$$

where θ is the angle between the magnetic field and a
vector joining the magnetic moments of the tantalum
nucleus and the electron. A and B are constants which
typically have the same sign. The expression for H goes
through a minimum at $\theta = 90^\circ$. This implies that the
electron charge density is concentrated in a plane normal
to the c axis, since the hyperfine pattern has the

smallest splittings for H parallel to the c axis.

This angular dependence analysis of the Ta^{4+} ESR spectrum suggests that the defect giving rise to the eight-line hyperfine pattern in $LiTaO_3$ is a 5d electron self-trapped on a Ta^{5+} ion. To first order, the d electron is in a plane perpendicular to the c axis.

Point Defects in Mg-doped $LiNbO_3$

Electron spin resonance spectra were taken from the as-grown $LiNbO_3$ crystals prior to the reduction and radiation treatments. Major differences were found in these spectra, as shown in Fig. 24. To facilitate comparisons, the samples used for Fig. 24 were the same size and the spectrometers's gain, microwave power, and modulation amplitude were kept constant. Each trace was taken at 77 K with the magnetic field parallel to the c axis. Trace (a) in Fig. 24 shows the ESR spectrum for undoped $LiNbO_3$; the dominant line at 790 G has been previously attributed to Fe^{3+}.[5-7] Homogeneous broadening, due to rapid spin-lattice relaxations, prevents the observation of ESR signals from Fe^{2+} ions that may be present in our crystals. The ESR spectrum for the 3%-doped stoichiometric sample is shown in trace (b) of Fig. 24. The normal Fe^{3+} signal, at 790 G, is smaller in intensity and is broadened relative to the undoped sample. The ESR data for the 5%-doped stoichiometric sample, shown in trace (c) of Fig. 24, is
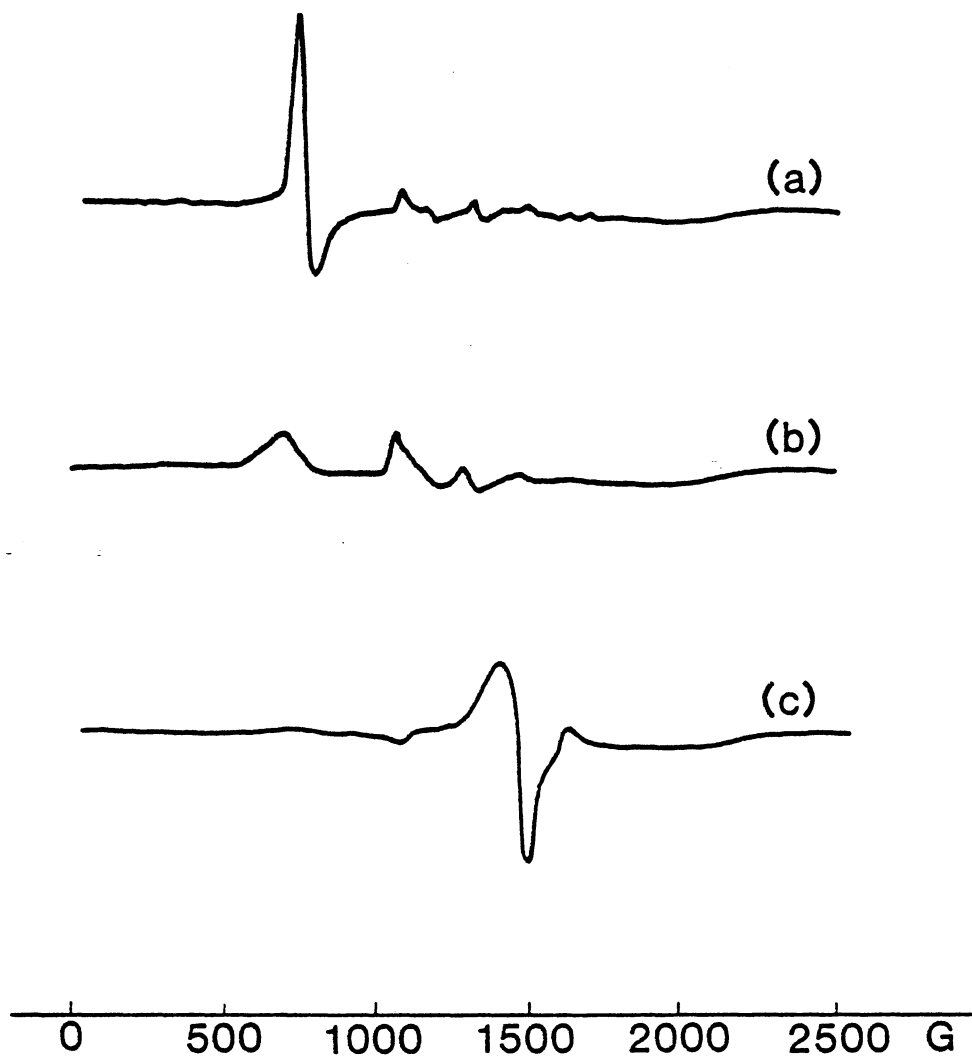
Figure 24. ESR spectra representing iron impurities in as-grown LiNbO$_3$. Trace (a) is from an undoped crystal, trace (b) is from a 3%-Mg-doped crystal, and trace (c) is from a 5%-Mg-doped crystal

significantly different from the undoped and 3%-doped crystals. The Fe^{3+} signal that was present in trace (a) and trace (b) is absent, but a prominent ESR line near 1500 G is observed.

Inductively coupled plasma (ICP) emission spectroscopy results indicate that a representative Mg-doped crystal had essentially the same Fe content (~7 ppm) as the undoped samples. An ESR spectrum from a 5%-Mg-doped, 100 ppm Fe-doped $LiNbO_3$ crystal had a dominate line at 1500 gauss, which is similar to trace (c) of Figure 24. Thus, the 1500 gauss line in trace (c) of Fig. 24 is assigned to Fe^{3+}. This suggests that the change in the Fe^{3+} ESR signal as the Mg-doping level increases, which is illustrated in Fig. 24, corresponds to Fe^{3+} occupying a different site in the crystal.

Radiation Effects

Ionizing radiation produces intense optical absorption bands in $LiNbO_3$. For reference, an absorption spectrum initially was taken at 10 K from the as-grown 5%-doped stoichiometric crystal and is shown in trace (a) of Fig. 25. The sample then was irradiated at 10 K with x-rays obtained from the Van de Graaff accelerator, and the optical absorption spectrum was taken again at 10 K with no intervening change in temperature. Two prominent absorption bands, near 500 nm and 1200 nm, were induced by this irradiation and are shown in trace (b) of Fig.
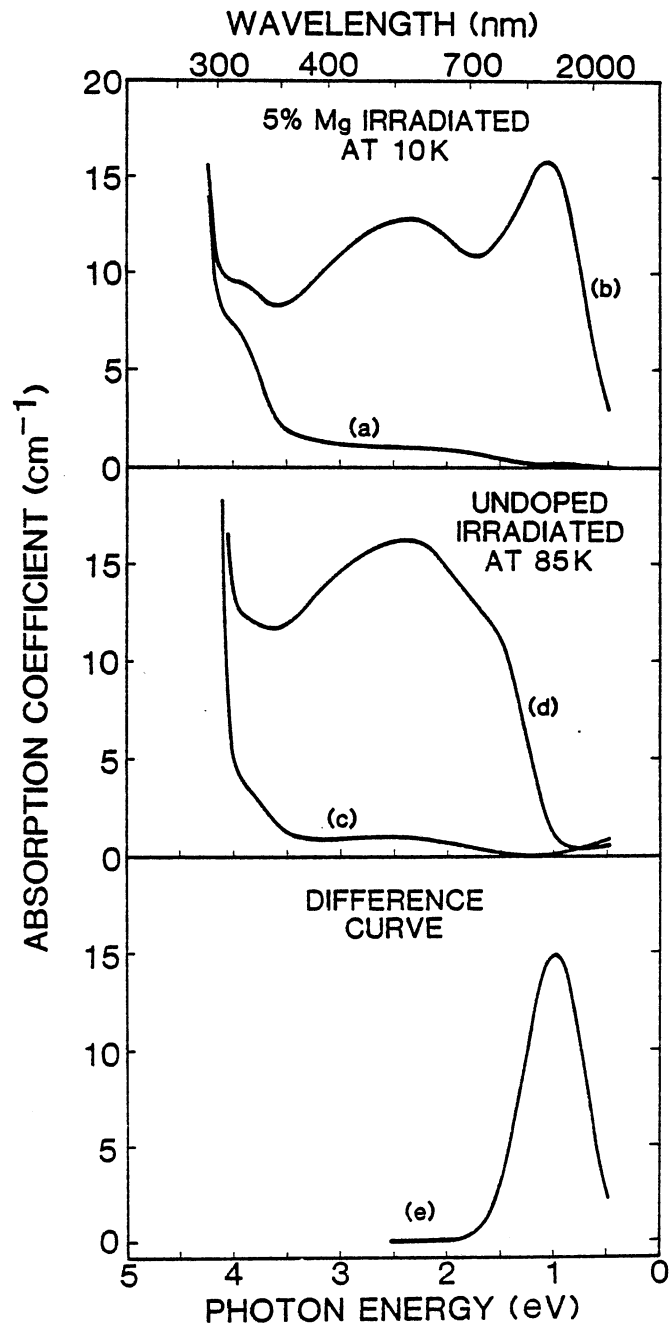
Figure 25. Comparison of radiation-induced optical absorption spectra from undoped and Mg-doped LiNbO₃ crystals

25. Similar radiation-induced optical absorption bands were observed in the 5%-doped congruent crystal. In view of the ESR data given below, it is suggested that the 500-nm band is due to a trapped-hole center and that the 1200-nm band may be due to an electron trap. This hypothesis is also supported by the work of Schirmer and von der Linde.[4]

Two ESR spectra, produced in both the 5%-doped stoichiometric and the 5%-doped congruent samples by low-temperature irradiation, appear to correlate with the optical spectra described in the preceding paragraph. The data in trace (a) of Fig. 26 was obtained at 15 K after the 5%-doped stoichiometric sample was irradiated at 77 K with x-rays from the Van de Graaff accelerator. In this case, the sample was cooled to 15 K directly after the 77-K irradiation. The c axis was parallel to the magnetic field and a modulation frequency of 200 Hz was used. There are two overlapping ESR spectra in trace (a), neither of which was present before the irradiation. The narrower, intense line labeled hole center is structureless and has a g_c value of 2.03. Also present is an unusually broad ESR signal which represents a large defect concentration. The extremes of this latter spectrum are marked by arrows and it has an approximate g_c value of 1.82. It is suggested that the holelike ESR spectrum is due to the same trapped-hole center responsible for the 500-nm band and that the electronlike
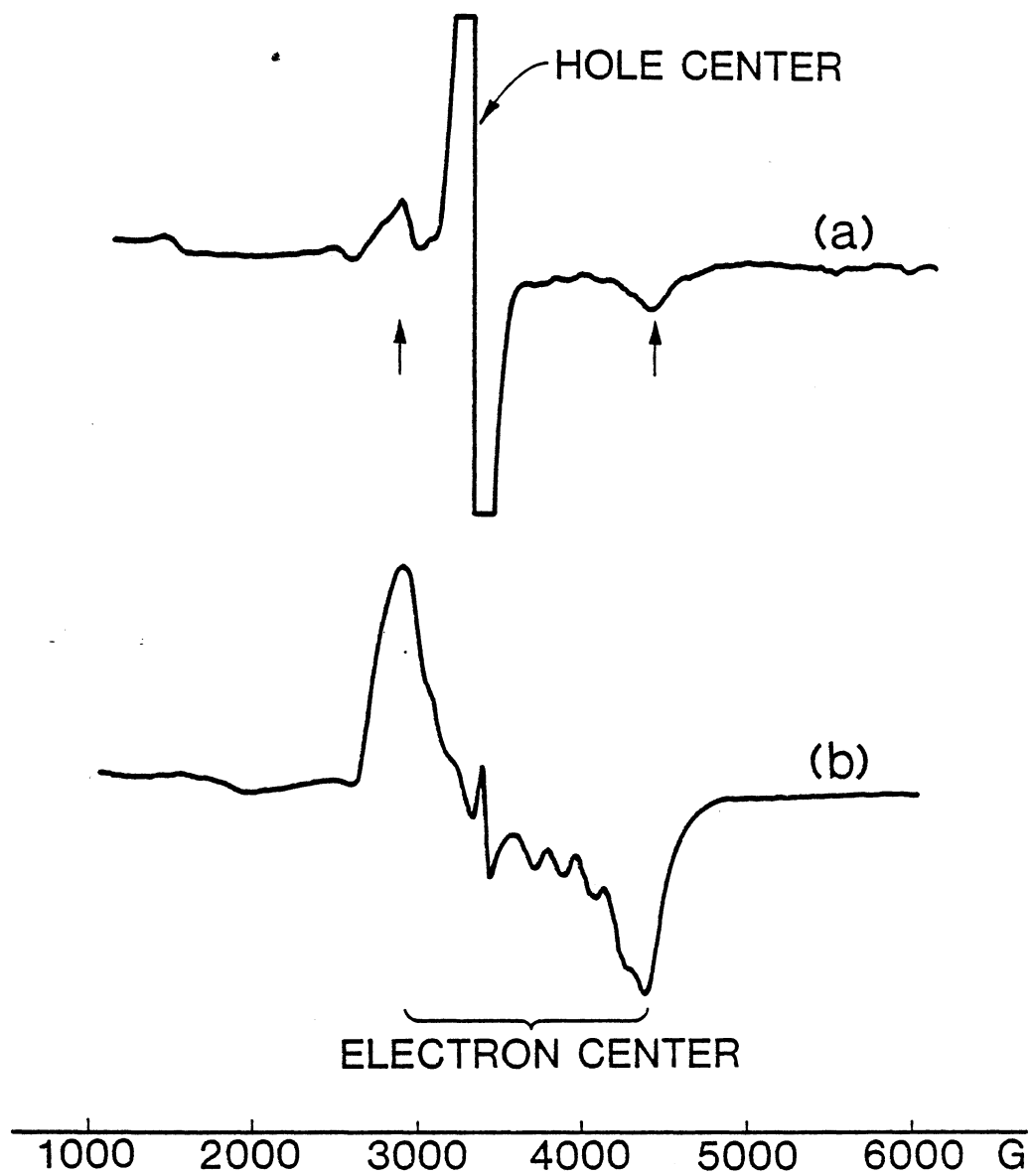
Figure 26. ESR spectra obtained from a 5%-Mg-doped LiNbO₃
crystal after separate (a) radiation and
(b) reduction experiments
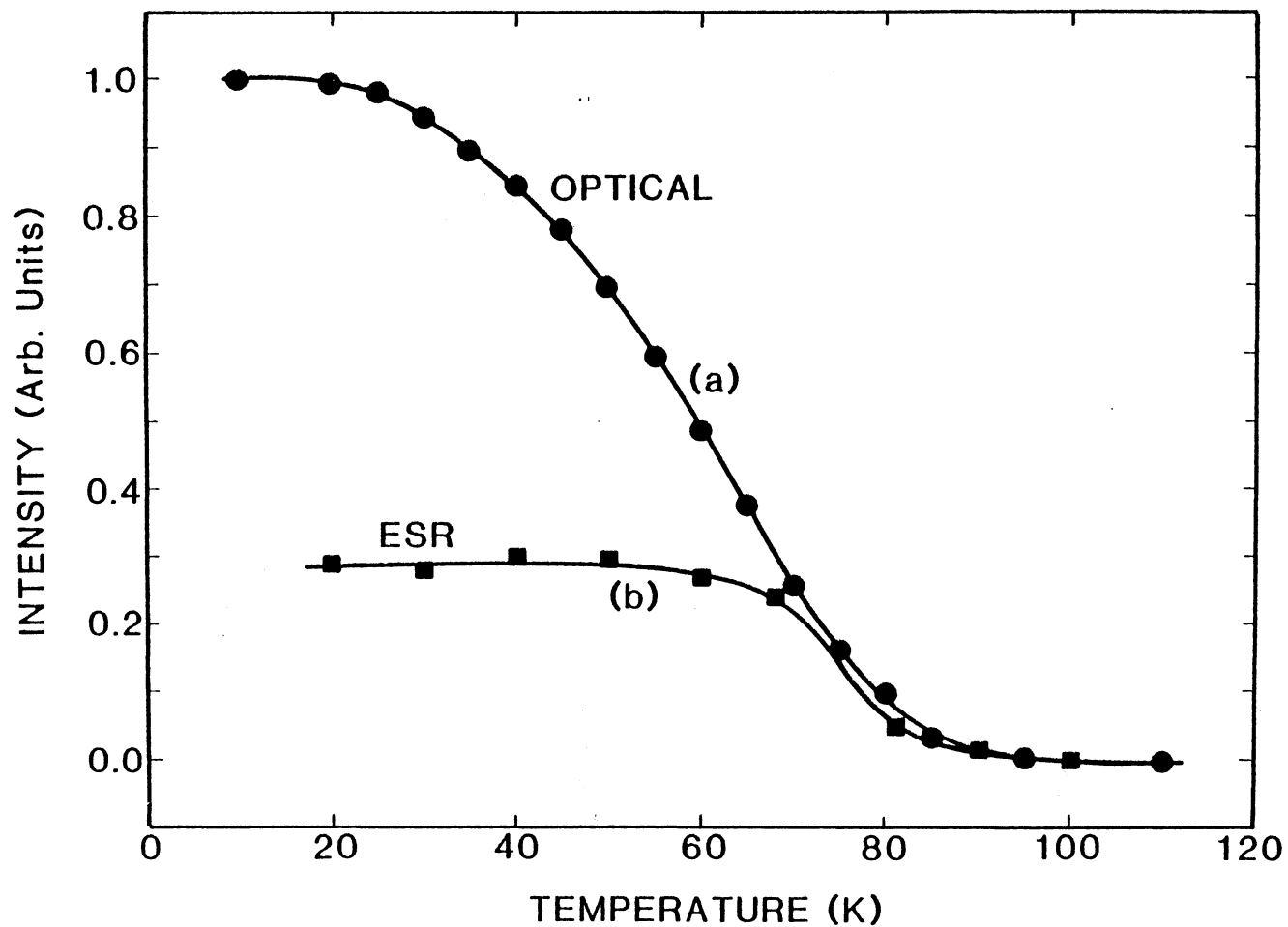
Figure 27. Thermal anneal of x-irradiated 5%-Mg-doped LiNbO$_3$. Trace
(a) is the 1200-nm optical band and trace (b) is from
the ESR hole center

ESR spectrum (at g_c = 1.82) is due to the electron trap responsible for the 1200-nm band.

The temperature stability of the radiation-induced 1200-nm band was determined for the 5%-doped stoichiometric crystal. Curve (a) in Fig. 27 shows the intensity of this band as the temperature is steadily increased at a rate of approximately 1 K/min. The responsible defect decays over the temperature range 20 to 100 K. A separate experiment to determine the temperature stability of the holelike center, induced by x-rays in the 5%-doped stoichiometric and the 5%-doped congruent samples, involved monitoring its ESR spectrum during a pulse-anneal sequence. The apparatus only permitted irradiations of the ESR samples at 77 K or above even though it was expected, from the 1200-nm band anneal data, that the relevant defects would be decaying substantially at these temperatures. Thus, the sample was irradiated at 77 K and then immediately cooled to 15 K. Each step of the subsequent pulse anneal consisted of holding the sample at the desired temperature for 5 minutes and then returning to 15 K where the intensity of the ESR spectrum was measured. The data indicates that the paramagnetic holelike center produced by the 77-K irradiation decays in the temperature range 60 to 90 K. Curves (a) and (b) of Fig. 27 represent different experiments, but they are presented together to show that the temperature dependence of the decay of the 1200-nm

absorption peak and of the ESR line (g_c = 2.03) are
similar above about 70 K. Since the irradiation for the
ESR experiment was carried out at 77 K, annealing at this
temperature has already occurred during the irradiation.
This is presumed to be the reason that the low-
temperature annealing in curve (b) is absent, and it also
explains why the intensity of the ESR spectrum (curve
(b)) was initialized to 0.3 units. The specific value of
0.3 was obtained from the ratio of integrated
thermoluminescence outputs (to be described later) over
the range 15 K to 110 K when preceded by irradiations at
77 K and at 15 K.

The undoped, the 3%-doped stoichiometric, and the
5%-doped Li-deficient crystals have radiation-induced
optical absorption spectra that are similar to each other
but different from that described for the previous two
samples. As an example, the optical absorption from the
undoped $LiNbO_3$ crystal is shown in trace (d) of Fig. 25.
This spectrum was taken at 85 K after irradiation at 85 K
with x-rays produced by the Van de Graaff accelerator.
Prior to the irradiation, no major optical bands were
observed in the undoped crystal, as illustrated in trace
(c) of Fig. 25. The 85-K irradiation temperature is
above the decay temperature for the 1200-nm band;
however, Arizmendi et al.[29] describe an optical
absorption spectrum produced by x-irradiation at 10 K in
undoped $LiNbO_3$ which is nearly identical to trace (d) in

Fig. 25. Thus, the principal feature in the radiation-induced spectrum from the undoped material is a broad band peaking near 500 nm, irrespective of whether the sample was irradiated at 10 K or 85 K, and there is no evidence of a band at 1200 nm. The ESR spectra produced by irradiation at 77 K in the undoped, the 3%-doped stoichiometric, and the 5%-doped Li-deficient crystals are similar to each other but are different from that previously described for the other two 5%-doped samples. Although their ESR spectra are not shown, the radiation produces both a holelike center and the Nb^{4+} center in the undoped and its two related crystals.

Finally, the existence of the 1200-nm optical absorption band in trace (b) of Fig. 25 can be more conclusively shown by the following procedure. The radiation-induced absorption for the undoped sample is subtracted from the radiation-induced absorption for the 5%-doped stoichiometric sample (i.e., trace (d) in Fig. 25 is subtracted from trace (b)). The only adjustment to the original data was to normalize trace (d) to trace (b) at 500 nm. The result of this subtraction, shown in trace (e) of Fig. 25, is a symmetrical band peaking at 1200 nm similar to that suggested by the initial data. The two absorption curves used to generate this isolated 1200-nm band represented by trace (e) were taken at different temperatures, but this has only a minor influence on the result.

Thermoluminescence (TL) was observed in several of the crystals, but not in others, when they were x-ray irradiated at 15 K and then warmed to room temperature. Specifically, the 5%-doped stoichiometric and the 5%-doped congruent crystals both showed a large TL emission at 70 K, whereas no emission was observed for the undoped, the 3%-doped stoichiometric, and the 5%-doped Li-deficient crystals in the temperature range 15 K to 300 K.

Trace (a) in Fig. 28 shows the TL data, taken with a heating rate of approximately 2 K/min, for the as-grown 5%-doped stoichiometric crystal after a 30-minute x-irradiation at 15 K. A monochromator was not used, therefore these results represent the panchromatic emission as a function of temperature. A single peak occurs near 70 K and has a halfwidth of approximately 40 K. After taking the data shown in trace (a), the sample was then reduced at 1000°C for one hour in a vacuum of 10^{-5} Torr. Following this reduction, the TL data shown in trace (b) of Fig. 28 were taken. The presence of a narrower TL peak in the reduced sample suggests that an unresolved contribution initially present in the as-grown crystal between 70 and 100 K, may have been removed by the reducing treatment. The wavelength dependence for the emission from the as-grown crystal was obtained at 65 K with 0.5-mm slit widths on the monochromator. This spectrum is shown in Fig. 29 to peak near 430 nm; the
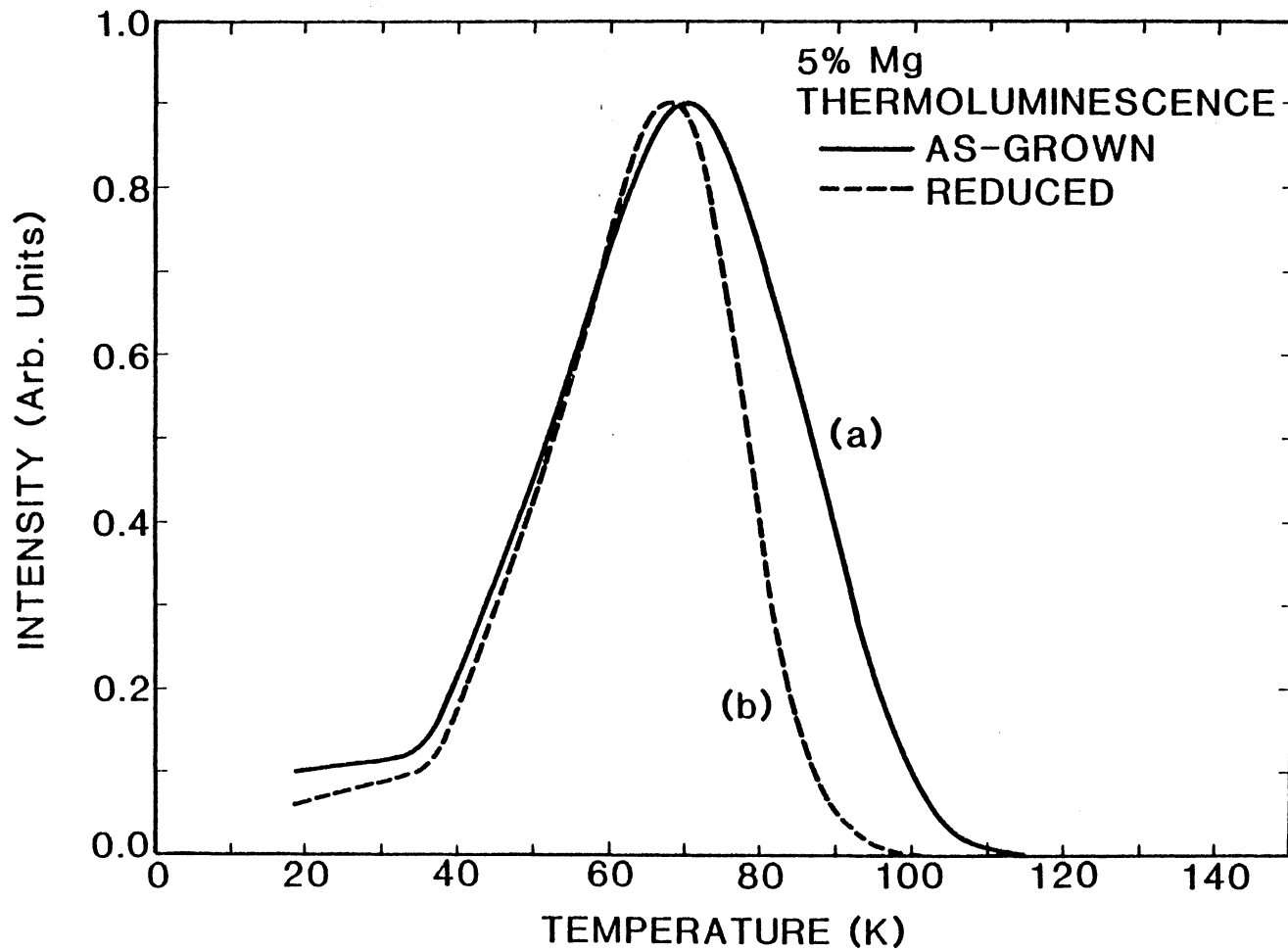
Figure 28. TL curves from a 5%-Mg-doped stoichiometric LiNbO$_3$ crystal
following x-ray irradiation at 15 K
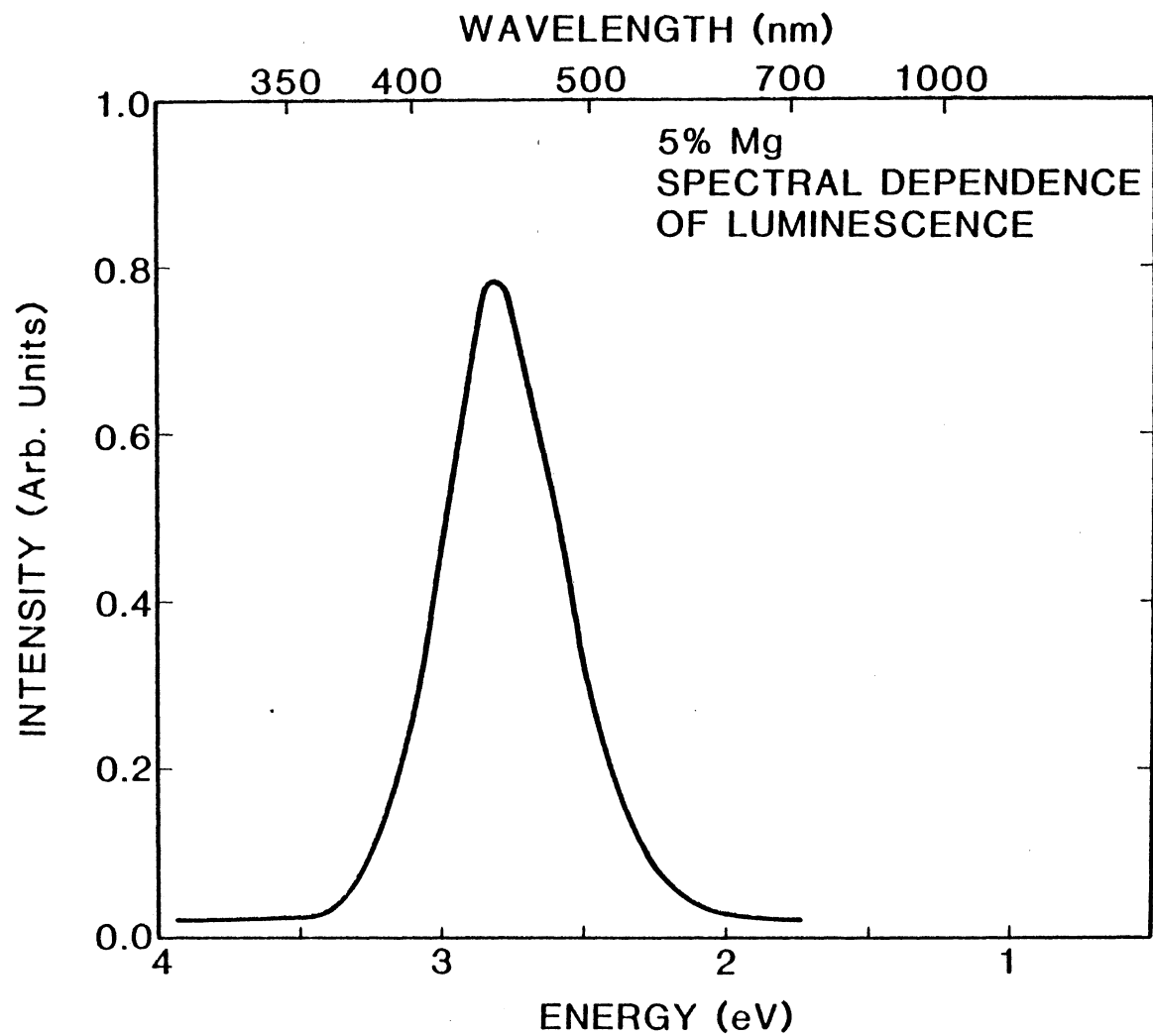
Figure 29. Spectral dependence of the TL emission from 5%-Mg-
doped stoichiometric LiNbO$_3$

same spectral dependence also was obtained at 45 K and 75 K. It is important to note that optical absorption and ESR spectra were observed to thermally decay near 70 K in these same samples which have a 70-K TL peak.

In addition to the TL observed in several of the crystals, there is a continuous luminescence produced directly by the x-rays in all of the samples. The intensity of this x-ray-induced luminescence (also known as radioluminescence) was investigated over the temperature range from 15 K to room temperature. Figure 30 is a comparison of the relative intensities of the panchromatic emission induced by the x-rays for the undoped, the 3%-doped stoichiometric, and the 5%-doped stoichiometric crystals. At 15 K, the intensity of the 5%-doped stoichiometric crystal was a factor of ten greater than the 3%-doped stoichiometric crystal and a factor of 100 greater than the undoped crystal. All three samples exhibited thermal quenching effects in the temperature range investigated. Also, the wavelength dependence of the x-ray-induced luminescence, at 15 K, is the same for all the Mg-doped samples, and it is identical to the TL dependence shown in Fig. 29. This same wavelength dependence has been reported by Arizmendi et al.[30] for the x-ray-induced luminescence from undoped lithium niobate at 15 K. The similarity of the wavelength dependence may indicate that the luminescence in all the samples is due to the same process, with the
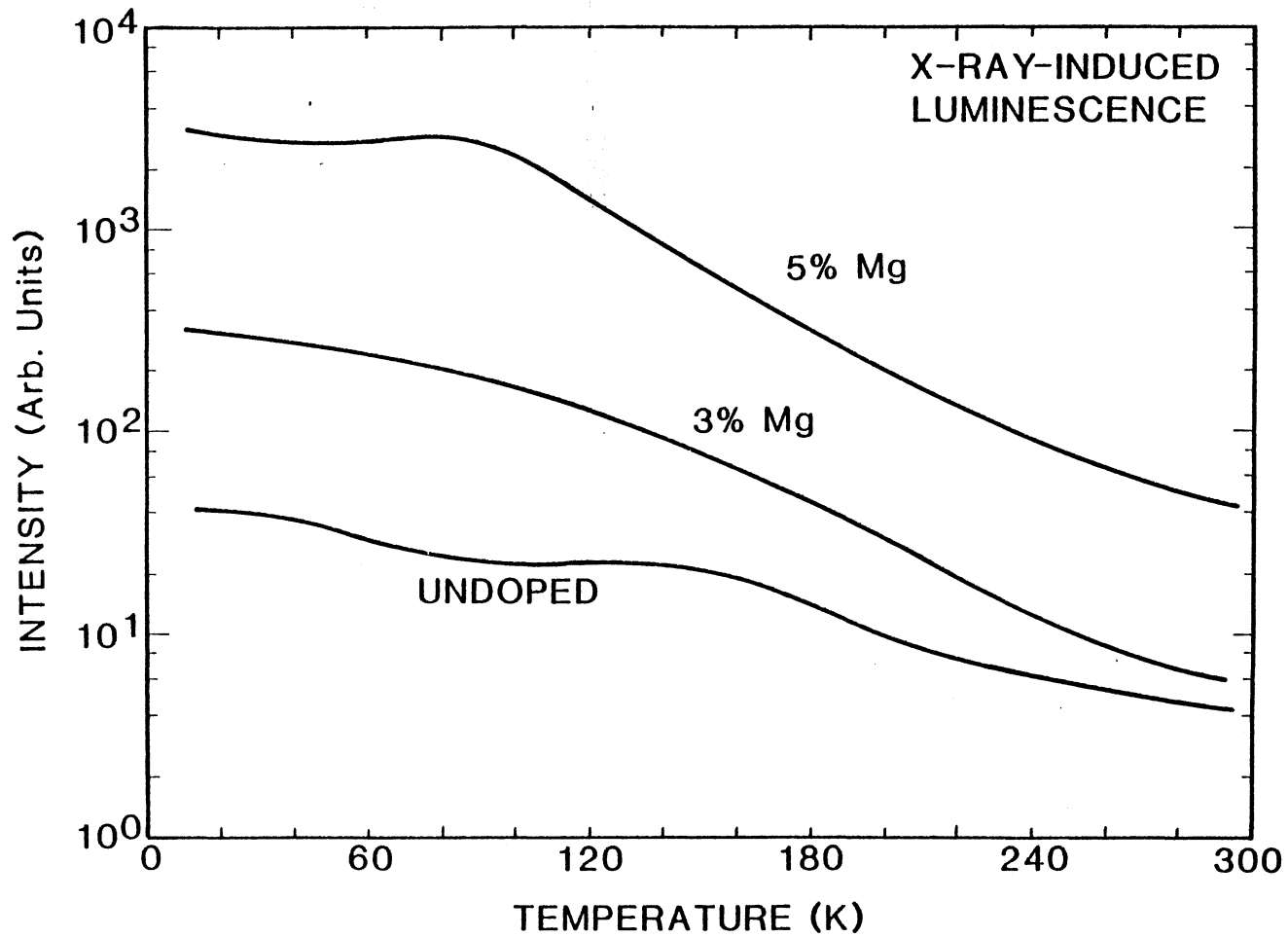
Figure 30.   Comparison of the relative intensities of the x-ray-induced
luminescence in undoped, 3%-Mg-doped, and 5%-Mg-doped
$LiNbO_3$

magnitude depending on the doping.

Reduction Effects

LiNbO$_3$ is easily reduced by heating to a high temperature in a vacuum, and a primary result of this process is the introduction of oxygen vacancies into the crystal. Undoped LiNbO$_3$ has an intense 500-nm optical absorption band after reduction at 1000°C in a vacuum of 1 x 10^{-5} Torr. Subsequent optical bleaching at 77 K causes this 500-nm band to decrease substantially and a 760-nm band to appear. This general behavior for the undoped LiNbO$_3$ has been described above. The same optical behavior was observed in the 3%-doped stoichiometric and the 5%-doped Li-deficient samples after similar vacuum reduction treatments. Figure 31 shows this data from the 3%-doped stoichiometric crystal; trace (a) is the 500-nm band present after reduction and trace (b) is the 760-nm band present after bleaching the reduced sample at 77 K. This latter band is unstable at room temperature.

Significantly different behavior, compared to the undoped material, was observed when the 5%-doped stoichiometric and 5%-doped congruent samples were reduced. Trace (a) in Fig. 32 shows the optical absorption at 77 K from the as-grown 5%-doped stoichiometric crystal prior to reducing. This sample
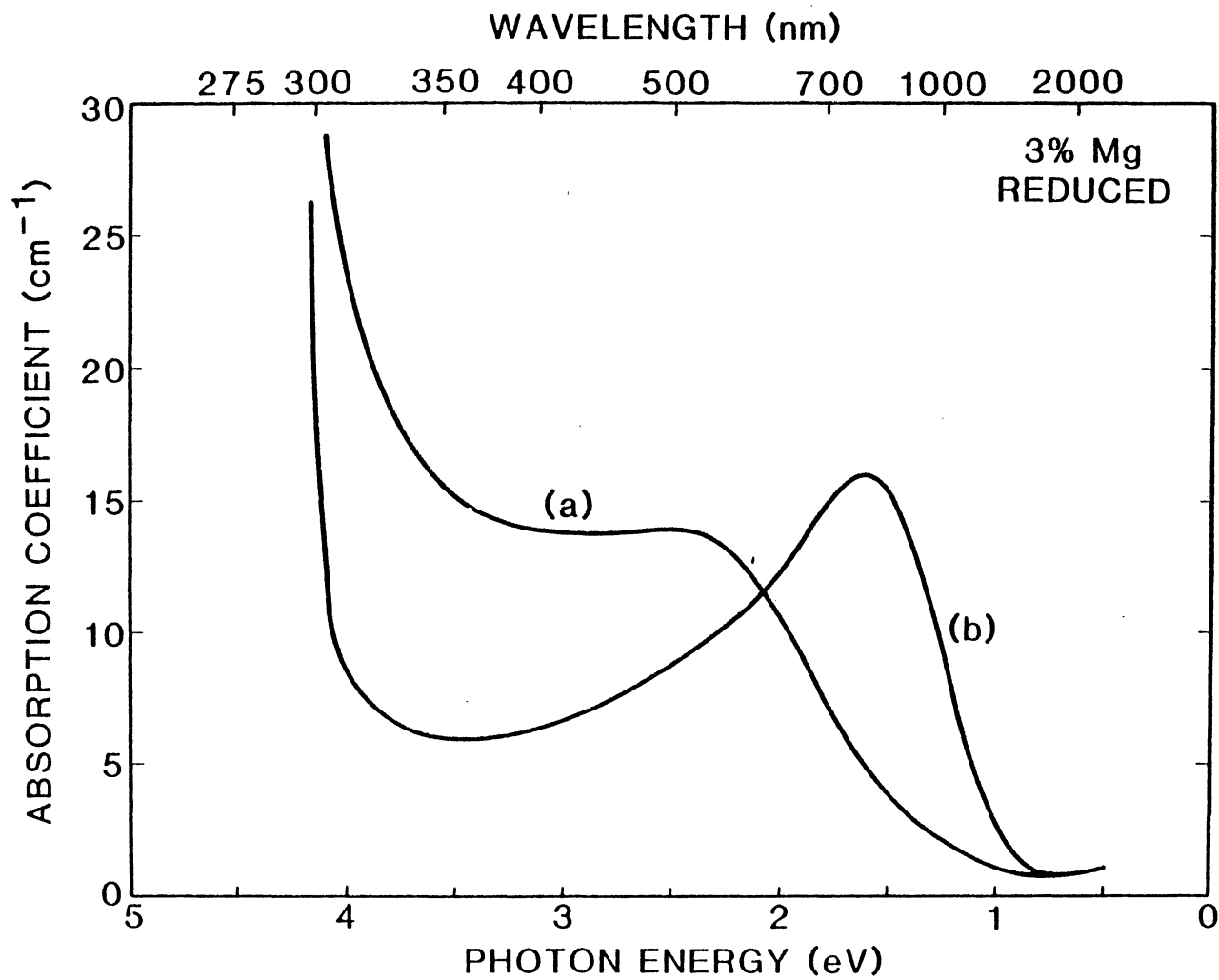
Figure 31. Optical absorption from a reduced 3%-Mg-doped LiNbO₃ crystal
(a) before and (b) after an 85 K optical bleach
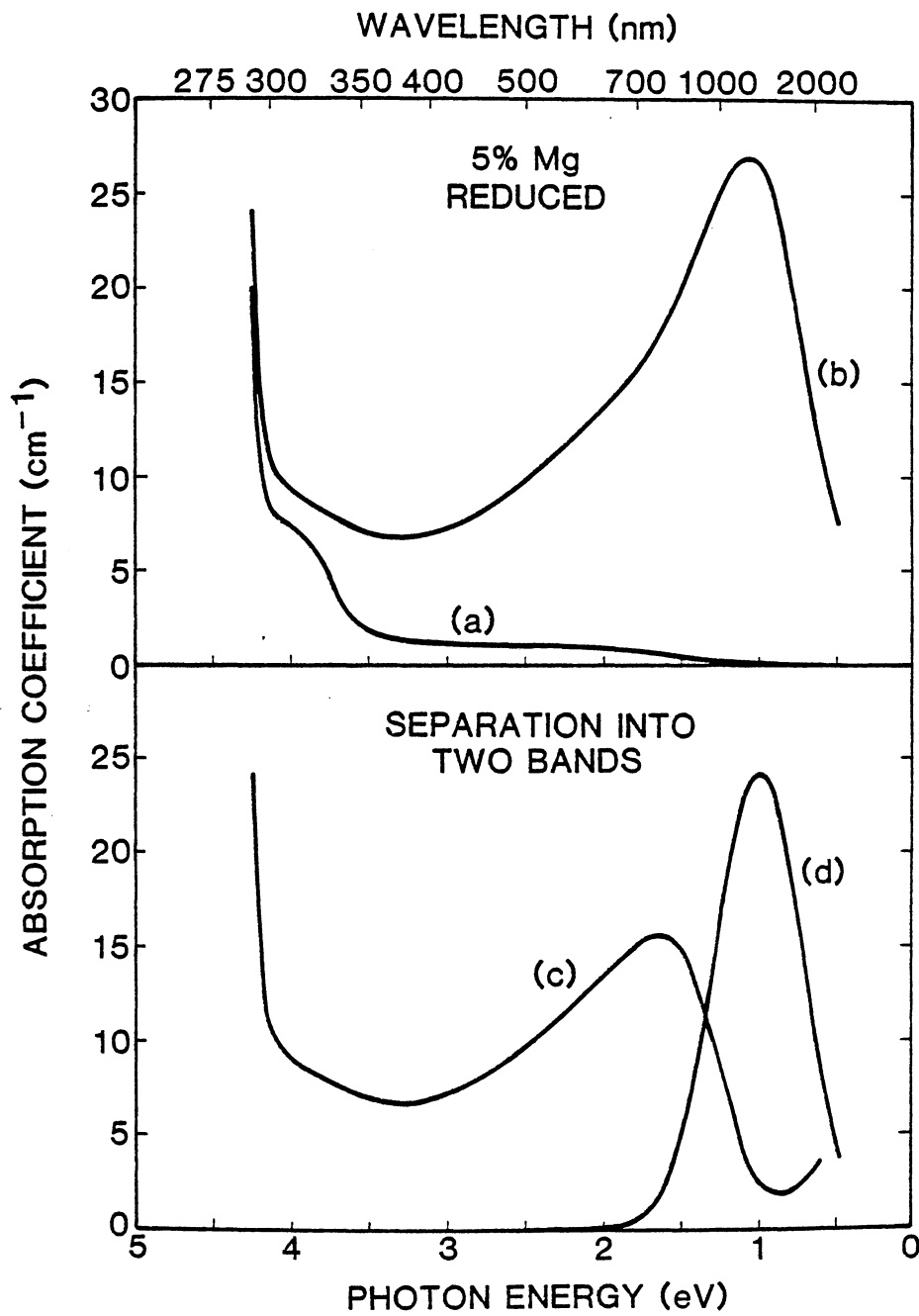
Figure 32. Optical absorption from a reduced
5%-Mg-doped stoichiometric $LiNbO_3$
crystal

was then heated to 1000°C for one hour in a vacuum of 1 x 10^{-5} Torr, and the resultant optical absorption is shown in trace (b) of Fig. 32. Subsequent optical bleaching near liquid nitrogen temperature had very little effect on this spectrum. The major features of the spectrum in trace (b) are a peak at 1200 nm accompanied by a slowly decreasing tail on the high-energy side. This shape for the absorption suggests that the spectrum can be decomposed into two bands by the following procedure. The 1200-nm band shape from trace (e) in Fig. 25, which was induced by x-rays in the 5%-doped stoichiometric crystal, is reproduced as trace (d) in Fig. 32. The peak magnitude of this band was chosen to be 0.9 of the peak intensity of trace (b) in Fig. 32. Then the 1200-nm band was subtracted from the total absorption induced by the reduction, which is represented by trace (b) in Fig. 32, and found that the remaining absorption formed a band peaking near 760 nm, as shown in trace (c) of Fig. 32. This 760-nm band resulting from the subtraction procedure appears to be identical in shape to the 760-nm band shown in trace (b) of Fig. 31, although the responsible defect is now stable at room temperature. It should be emphasized that the isolation of optical bands has not involved making a priori assumptions about their individual shapes.

The reduced 5%-doped stoichiometric crystal described in the previous paragraph exhibited an intense

ESR spectrum that has the same thermal stability as the induced optical bands at 760 and 1200 nm. This spectrum, which is shown in trace (b) of Fig. 26 and labeled electron center, was obtained at 15 K and consists of a broad set of overlapping lines with an approximate g_c value of 1.82. A similar ESR spectrum was observed in the 5%-doped congruent crystal, but not in the undoped, the 3%-doped stoichiometric, and the 5%-doped Li-deficient crystals. The spectrum in trace (b) appears to be identical to the broad spectrum denoted by arrows in trace (a) of Fig. 26. Thus it appears that the two spectra are the same, i.e., the low temperature irradiation and the vacuum reduction produce the same defect.

CHAPTER IV

DISCUSSION

The present investigation has provided information about point defects produced by radiation and reduction in a series of undoped $LiNbO_3$, undoped $LiTaO_3$, and Mg-doped $LiNbO_3$ crystals.

It was found that the same types of defects are formed in undoped $LiNbO_3$ and $LiTaO_3$ by radiation and reduction. X-irradiation at 77 K produces trapped hole centers and electrons trapped at Nb^{5+} and Ta^{5+} ions which can be monitored by ESR. The thermal stability for these irradiation produced centers is similar since the decay of the defects was observed in the 100 K to 150 K region in both materials. One interesting difference between the two materials is the splitting in the ESR hole center spectrum shown in Fig. 6 for $LiTaO_3$ which was not observed in Fig. 3 for $LiNbO_3$. This splitting suggests that the hole center in $LiTaO_3$ is interacting with a proton, whereas the hole center in $LiNbO_3$ does not show any splitting. The same type of electron trap is observed in both materials after the x-irradiation at 77 K, that is, the Nb^{4+} in $LiNbO_3$ and the Ta^{4+} in $LiTaO_3$. The axial symmetry of the ESR patterns indicate a self-

trapped electron in each case. The angular dependence of the Ta^{4+} is slightly different than for the Nb^{4+}. The Ta^{4+} hyperfine pattern collapses to one observed line when the magnetic field is parallel to the c axis, as shown in Fig. 6, whereas the 10 lines of the Nb^{4+} pattern are resolved at the same orientation. The splitting of the hyperfine pattern mainly consists of two parts, an isotropic part due to electronic overlap at the nucleus and an anisotropic part due to a magnetic dipole-dipole interaction between the magnetic moments of the nucleus and the electron. The differences observed in the hyperfine splittings are mainly a result of the different occupied shells for the two cations, that is, the 4d electron of Nb^{4+} and the 5d electron in Ta^{4+}. The Nb^{4+} is observed to have more electronic overlap at the nucleus than Ta^{4+} as indicated by the more isotropic angular dependence.

The result of reduction treatments on undoped $LiNbO_3$ and $LiTaO_3$ also exhibited similar defects. The reduction causes similar changes in the valence state of impurities in the two materials, as shown in Fig. 10 for $LiNbO_3$ and Fig. 12 for $LiTaO_3$. Oxygen vacancies, or F centers, characterized by a broad optical absorption band at 500 nm in $LiNbO_3$ and at 470 nm in $LiTaO_3$, are formed in both materials by heavy reductions. The oxygen vacancy formation is reversible for both materials by heating in an oxygen atmosphere. Crystals of $LiNbO_3$ and $LiTaO_3$

containing F centers exhibit F to F^+ conversion. That
is, if a reduced crystal of $LiNbO_3$ or $LiTaO_3$ is cooled to
77 K and bleached, one of the electrons from the oxygen
vacancy is excited out of the vacancy and is trapped at
either the Nb^{5+} or the Ta^{5+}, respectively. After the F
to F^+ conversion, an ESR spectrum for both the F^+ center
and the Nb^{4+} ion or the Ta^{4+} ion is expected. The Nb^{4+}
ion and the Ta^{4+} ion spectra are observed, as shown in
Fig. 17 and Fig. 19, but the F^+ center is apparently
broadened by interaction with the surrounding nuclei and
hence unobservable.

After the F to F^+ conversion, an optical absorption
band for the F^+ center and the Nb^{4+} or Ta^{4+} are expected.
Two distinct bands are not present, as shown by the
polarized optical absorption after the conversion in Fig.
20 for $LiNbO_3$ and Fig. 21 for $LiTaO_3$. Since the bands
are apparently overlapping, an assignment cannot be made
from the reduction data. Although the x-irradiation
data, where both hole center and either Nb^{4+} or Ta^{4+}
absorption would be expected, suggests that the Nb^{4+} and
Ta^{4+} have absorption in the 1.4 eV to 1.5 eV region.
That is, the shoulder on the optical absorption curves at
1.5 eV in Fig. 2 for $LiNbO_3$ and at 1.4 eV in Fig. 5 for
$LiTaO_3$ is possibly due to the Nb^{4+} ion and the Ta^{4+} ion,
respectively.

Two important conclusions are indicated by an
analysis of the point defects produced by radiation and

reduction in the Mg-doped $LiNbO_3$. First, the existence of a threshold Mg-doping level and second, an electron trap which occurs only in samples above that threshold. The $LiNbO_3$ samples are divided into two groups. Those in the first group, which are arbitrarily labeled Type I, are the undoped $LiNbO_3$, the 3%-doped stoichiometric and the 5%-doped Li-deficient crystals. The second group, labeled Type II, consists of the 5%-doped stoichiometric and the 5%-doped congruent crystals. This separation of the samples into two groups, with no gradual transition occurring between their different behaviors, implies a threshold.

The distinction between Type I and Type II samples depends on two parameters. One parameter is the magnesium doping level and the other is the lithium vacancy concentration in the sample. The lithium vacancy concentration was indicated by the stoichiometry of the $LiNbO_3$ crystal, that is either stoichiometric (50% Li in the melt), congruent (48.6% Li in the melt), or Li-deficient (46.5% Li in the melt). A summary of the estimated concentrations of magnesium ions and lithium vacancies for the five different $LiNbO_3$ crystals used is presented in Table II. Also listed in Table II is whether the sample is above or below threshold.

The magnesium-doping-level parameter is indicated by the behavior of the three stoichiometric samples with 0, 3%, and 5% MgO in the melt, with only the 5%-Mg-doped

TABLE II

A SUMMARY OF THE ESTIMATED CONCENTRATIONS OF MAGNESIUM
IONS AND LITHIUM VACANCIES FOR THE FIVE LITHIUM NIOBATE
CRYSTALS

Mg CONCEN-TRATION	TYPE OF MELT	Li-VACANCY CONCENTRATION	BEHAVIOR OBSERVED
0%	CONGRUENT	3%	BELOW THRESHOLD
3%	STOICHIOMETRIC	3%	BELOW THRESHOLD
5%	Li-DEFICIENT	5%	BELOW THRESHOLD
5%	STOICHIOMETRIC	3%	ABOVE THRESHOLD
5%	CONGRUENT	3%	ABOVE THRESHOLD

crystal being above threshold. The lithium-vacancy-concentration parameter is indicated by the different behaviors of the Type I 5%-Mg-doped Li-deficient crystal and the Type II 5%-Mg-doped stoichiometric crystal. Although the Mg-doping level is the same for these two crystals, their concentrations of lithium vacancies are not the same. The samples which showed below-threshold behavior had lithium vacancy concentrations higher than or similar to the magnesium level. Conversely, above-threshold behavior was found only in samples where the magnesium ions significantly exceeded the number of lithium vacancies. Thus, the threshold doping level (i.e., defined to be production of the 1200-nm optical absorption band during reduction) depends directly on the ratio of magnesium ions to lithium vacancies.

Thus, the data indicate that the threshold level depends upon both the magnesium concentration and the lithium-vacancy concentration. The divalent charge of the magnesium suggests that this ion occupies a lithium site in $LiNbO_3$. Because of their excess positive charge relative to this lattice site, these substitutional Mg^{2+} ions can act as charge compensators for lithium vacancies which are present in the crystal at high (up to 3%) concentrations.[31] Since the lithium vacancy concentration is normally very large, early investigators proposed that the charge compensation in undoped $LiNbO_3$ is accomplished by "anti-site" niobium ions, either via a

simple one-for-one substitution[32] or through replacement of extended sequences of ions.[12] The off-site niobium ions are no longer needed for charge compensation of the lithium vacancies when the Mg^{2+} ions are present. This means that the lithium vacancy concentration can stay constant and the off-site niobium concentration can decrease as magnesium is added to the crystal.

The Mg^{2+} ion on a lithium site results in an effective positive charge relative to the lattice. When electrons are released in the Type II crystals during irradiation or reduction, these substitutional Mg^{2+} ions can act as a trapping site. To a first-order approximation, such a defect is refered to as a Mg^{+} complex. The trapped electron within this defect is expected to be delocalized onto a number of surrounding ions, thus justifying the label of "Mg^{+} complex" instead of simply a Mg^{+} ion. Also, there could be an additional defect near the Mg ion which aids in the stabilization of the trapped electron. Therefore, the 1200-nm optical band of Fig. 25 and Fig. 32, which was formed by x-irradiation and reduction in Type II $LiNbO_3$, is assigned to the Mg^{+} complex.

Table III is a summary of the present spectroscopic results for defects in $LiNbO_3$. The spectral features, method of production, and other comments are listed in the table for each of the major defects, and the relationship of each defect to the threshold effect is

indicated by specifying whether the defect is observed in Type I or Type II material. Radiation-induced trapped hole centers are produced in both Type I and Type II material, although their behaviors are slightly different in the two cases. The hole center in Type I material has an absorption peak at 500 nm, an ESR spectrum with $g_c =$ 2.03, and it thermally decays in the 100 K to 150 K range. The hole center in Type II material is similar except it thermally decays well below 100 K.

Oxygen vacancies are formed in both Type I and Type II crystals during reduction, but there is again a significant difference in their behavior for the two materials. The excess positive charge of the Mg^{2+} ion on a lithium site provides a stable trap at room temperature. Hence, after reduction, the oxygen vacancies in Type II material are in the form of F^+ centers with the electron trapped on the Mg^{2+} ion.

The point defects produced in $LiTaO_3$ are similar to those defects produced in $LiNbO_3$. A summary of the defects produced by radiation or reduction in $LiTaO_3$ are presented in Table IV.

TABLE III

A SUMMARY OF POINT DEFECTS PRODUCED IN LITHIUM NIOBATE
DURING RADIATION OR REDUCTION EXPERIMENTS

DEFECT	SPECTRAL FEATURE	METHOD OF PRODUCTION	MATERIAL TYPE	COMMENTS
HOLE CENTER (O^- ION AND ADJACENT DEFECT)	ABSORPTION AT 500 nm	RADIATION	I	DECAYS NEAR 150 K
	ESR LINE AT g_c = 2.03	RADIATION	I	DECAYS NEAR 150 K
	ABSORPTION AT 500 nm	RADIATION	II	DECAYS NEAR 70 K
	ESR LINE AT g_c = 2.03	RADIATION	II	DECAYS NEAR 70 K
F CENTER	ABSORPTION AT 500 nm	REDUCTION	I	STABLE AT RT
F^+ CENTER	ABSORPTION NOT ASSIGNED	REDUCTION	I	FORMED BY BLEACH AT 77 K
	ESR SPECTRUM NOT OBSERVED	REDUCTION	I	FORMED BY BLEACH AT 77 K
	ABSORPTION NOT ASSIGNED	REDUCTION	II	STABLE AT RT
	ESR SPECTRUM NOT OBSERVED	REDUCTION	II	STABLE AT RT

TABLE III (continued)

DEFECT	SPECTRAL FEATURE	METHOD OF PRODUCTION	MATERIAL TYPE	COMMENTS
Nb^{4+}	ESR SPECTRUM AT $g_c = 1.90$	RADIATION	I	DECAYS NEAR 150 K
	ABSORPTION NOT ASSIGNED	RADIATION	I	DECAYS NEAR 150 K
	ESR SPECTRUM AT $g_c = 1.90$	REDUCTION	I	FORMED BY BLEACH AT 77 K
	ABSORPTION NOT ASSIGNED	REDUCTION	I	FORMED BY BLEACH AT 77 K
Mg^+ COMPLEX	ABSORPTION AT 1200 nm	RADIATION	II	DECAYS NEAR 70 K
	ESR SPECTRUM AT $g_c = 1.82$	RADIATION	II	DECAYS NEAR 70 K
	ABSORPTION AT 1200 nm	REDUCTION	II	STABLE AT RT
	ESR SPECTRUM AT $g_c = 1.82$	REDUCTION	II	STABLE AT RT

TABLE IV

A SUMMARY OF POINT DEFECTS PRODUCED IN LITHIUM TANTALATE
DURING RADIATION OR REDUCTION EXPERIMENTS

DEFECT	SPECTRAL FEATURE	METHOD OF PRODUCTION	COMMENTS
HOLE CENTER (O^- ION AND ADJACENT DEFECT)	ABSORPTION AT 470 nm	RADIATION	DECAYS NEAR 150 K
	ESR SPECTRUM AT g_c = 2.02	RADIATION	DECAYS NEAR 150 K
F CENTER	ABSORPTION AT 470 nm	REDUCTION	STABLE AT RT
F^+ CENTER	ABSORPTION NOT ASSIGNED	REDUCTION	FORMED BY BLEACH AT 77 K
	ESR SPECTRUM NOT OBSERVED	REDUCTION	FORMED BY BLEACH AT 77 K
Ta^{4+}	ABSORPTION NOT ASSIGNED	RADIATION	DECAYS NEAR 150 K
	ESR SPECTRUM AT g_c = 1.47	RADIATION	DECAYS NEAR 150 K
	ABSORPTION NOT ASSIGNED	REDUCTION	FORMED BY BLEACH AT 77 K
	ESR SPECTRUM AT g_c = 1.47	REDUCTION	FORMED BY BLEACH AT 77 K

REFERENCES

1.   Zachariasen, W. H., Skr. Norske Vid.-Ada., Oslo,
         Mat. Naturv. No. 4 (1928).

2.   Ballman, A. A., J. Am. Ceram. Soc. $\underline{48}$, 112 (1965).

3.   Glass, A. M., G. E. Peterson, and T. J. Negran, in
         <u>Laser Induced Damage in Optic Materials</u>, Natl.
         Bur. Std. Special Publication No. 372, ed, A.
         J. Glass (US GPO, Washington D.C., 1972).

4.   Schirmer, O. F. and D. von der Linde, Appl. Phys.
         Lett. $\underline{33}$, 35 (1978).

5.   Towner, H. H., Y. M. Kim and H. S. Story, J. Chem.
         Phys. $\underline{56}$, 3676 (1972).

6.   Herrington, J. B., B. Dischler and J. Schneider,
         Solid State Commun. $\underline{10}$, 509 (1972).

7.   Mehran, F. and B. A. Scott, Solid State Commun. $\underline{11}$,
         15 (1972).

8.   Takeda, T., A. Watanabe and K. Sugihara, Phys. Lett.
         $\underline{27A}$, 114 (1968).

9.   Petrov, M. P., Sov. Phys. Solid State $\underline{10}$ 2574
         (1969).

10.   Rexford, D. G. and Y. M. Kim, Phys. Lett. $\underline{35A}$, 215
         (1971).

11.   Rexford, D. G. and Y. M. Kim, J. Chem. Phys. $\underline{57}$ 3094
         (1972).

12.   Nassau, K. and M. E. Lines, J. Appl. Phys. $\underline{41}$, 533
         (1970).

13.   Jorgensen, P. J. and R. W. Bartlett, J. Phys. Chem.
         Solids $\underline{30}$, 2639 (1969).

14.   Smith, R. G., D. B. Fraser, R. T. Denton, and T. C.
         Rich, J. Appl. Phys. $\underline{39}$, 4600 (1968).

15. Bryan, D. A., Robert Gerson, and H. E. Tomaschke, Appl. Phys. Lett. 44, 847 (1984).

16. Chen, C. Y., K. L. Sweeney, and L. E. Halliburton, Phys. Stat. Sol. (a) 81, 253 (1984).

17. Courths, R., P. Steiner, H. Hochst and S. Hufner, Appl. Phys. 21, 345 (1980).

18. Bollmann, W. and M. Gernand, Phys. Stat. Sol. 9a, 301 (1972).

19. Ohmori, Y., Y. Yasojima, and Y. Inuishi, Japan. J. Appl. Phys. 14 1291 (1975).

20. Ho, F. D., Phys. Stat. Sol. 66a 793 (1981).

21. Herrington, J. B., B. Dischler, A. Rauber and J. Schneider, Solid State Commun. 12 351 (1973).

22. Herrington, J. B., B. Dischler, and J. Schneider, Solid State Commun. 10, 509 (1972).

23. Burns, G., D. F. O'Kane, and R. S. Title, Phys. Rev. 167, 314 (1968).

24. Ketchum, J. L., K. L. Sweeney, L. E. Halliburton, and A. F. Armington, Phys. Lett. A94, 450 (1983).

25. Sweeney, K. L. and L. E. Halliburton, Appl. Phys. Lett. 43, 336 (1983).

26. Henderson, B. and J. E. Wertz, Defects in the Alkaline Earth Oxides (Taylor & Francis, London, 1977).

27. Lee, K. H. and J. H. Crawford, Jr., Phys. Rev. B 19, 3217 (1979).

28. La, S. Y., R. H. Bartram, and R. T. Cox, J. Phys. Chem. Solids 34, 1079 (1973).

29. Arizmendi, L., J. M. Cabrera, and F. Agullo-Lopez, J. Phys. C 17, 515 (1984).

30. Arizmendi, L., J. M. Cabrera, and F. Agullo-Lopez, Solid State Commun. 40, 583 (1981).

31. Lines, M. E. and A. M. Glass, Principles and Applications of Ferroelectric and Related Materials (Oxford University Press, Oxford, 1977).

32. Lerner, P., C. Legres, and J. P. Dumas, J. Crystal Growth 3/4, 231 (1968).

2

VITA

Kevin Lee Sweeney

Candidate for the Degree of

Doctor of Philosophy

Thesis: OPTICAL AND MAGNETIC RESONANCE CHARACTERIZATION
OF POINT DEFECTS IN LITHIUM NIOBATE AND LITHIUM
TANTALATE

Major Field: Physics

Personal Data: Born in Thomas, Oklahoma, April 28, 1957.

Education: Graduated from Thomas High School in 1975.
Received a Bachelor of Science degree from Oklahoma
State University in May, 1980. Entered Graduate
School at Oklahoma State University in 1980 and
received the Doctor of Philosophy degree in
December, 1984.

Experience: Graduate Teaching Assistant and Graduate
Research Assistant, Oklahoma State University,
Stillwater, Oklahoma, 1980-1984.